Process Monitoring of Fused Filament Fabrication

Noah Ferrarotto

Department of Mechanical Engineering

McGill University, Montreal

A thesis submitted to McGill University

in partial fulfillment of the requirements of the degree of

Master of Science

May 2022

ABSTRACT

3D printing of structures using fused filament is rapidly growing in industrial use. This thesis is motivated by the aerospace industry's desire to adopt fused filament fabrication (FFF) as a cost-effective process for manufacturing non-critical flying parts. Before aerospace companies can produce structural components using this technique, they must first overcome the barrier of certification. To be sold commercially, aerospace-grade parts must be demonstrated to perform equally well as the witness samples tested by the manufacturer. A promising strategy to guarantee this equivalency is to monitor process conditions and ensure their repeatability. Inter-layer tensile strength (or weld strength) is identified as a critical property of printed parts and an indicator of process repeatability. Its dependency on print parameters is examined by monitoring the thermal gradient and layer time during printing. Vertical dogbone coupons are used as witness samples to measure the weld strength for varying thermal gradients. It was found that shorter layer times caused steeper thermal gradients which in turn resulted in higher inter-layer weld strength.

RÉSUMÉ

L'impression 3D par filament fondu connait présentement une croissance rapide en industrie. Ce mémoire est propulsé par le désir de l'industrie aérospatiale d'adopter la fabrication par filament fondu (FFF) pour produire des pièces d'avion non-critiques à coût concurrentiel. Avant qu'une compagnie puisse produire des pièces structurales à l'aide de cette technique, elle doit d'abord surmonter la barrière de la certification. Afin d'être vendue commercialement, une pièce de qualité aérospatiale doit être démontrée comme étant aussi performante que les pièces témoins testées par le fabricant. Une stratégie prometteuse pour garantir cette équivalence est de mesurer les paramètres de procédé et d'en assurer la répétabilité. La résistance inter-couche est identifiée comme propriété critique d'une pièce imprimée et indicatrice de répétabilité du procédé. Sa dépendance aux paramètres d'impression est examinée en mesurant le gradient de température et le temps de couche pendant l'impression. Des éprouvettes de traction imprimées à la verticale sont utilisées comme témoins pour mesurer la résistance inter-couche pour différents gradients de température. Il fut déterminé que des temps de couche plus courts causaient des gradients de température plus prononcés, ayant pour effet d'augmenter la résistance inter-couche.

ACKNOWLEDGEMENTS

I above all wish to extend my gratitude to my supervisor Prof. Pascal Hubert welcoming me to his lab, first as an undergraduate and now as a master's student. His guidance was invaluable to my growth as a researcher and to the success of this project. I am happy to have had him as a mentor sharing my passion for composites and sailing.

I want to thank our industrial partners for integrating me to their research and development team. Their commitment to the project encouraged me to find the best possible way to carry out the research. I also wish to highlight my appreciation for the work of their technician with the mechanical testing.

To my colleagues Joshua, Farimah, Henri and all members of the McGill Structures and Composite Materials Laboratory (MSCML), thank you for your advice, questions and comments which pushed me to become a better researcher and science communicator.

I am grateful for the funding from the Research Centre for High Performance Polymers and Composites (CREPEC), the Natural Sciences and Engineering Research Council (NSERC), PRIMA Quebec and our industrial partner whose resources were indispensable to the completion of this project.

Lastly, thank you to my friend, colleague, and former supervisor Dr. Derek Harvey. It was him who introduced me to the world of research back in 2019 and got me to think about the power of mixing 3D printing and composite materials.

CONTENTS

LIST OF FIGURES

List of Tables

1 INTRODUCTION

Fused filament fabrication (FFF) has seen rapid growth in recent years due to the development of machines and materials able to compete with traditional processes like injection and compression moulding on a cost and performance basis. The aerospace industry is now looking to produce structural components using this technique. Aerospace part suppliers want to provide cost-effective components for their clients. Brackets and enclosures are promising candidates for FFF production as their complex geometry and low volume requirements to make FFF more suitable than injection moulding and CNC machining.

The main hurdle currently faced by FFF in aerospace is certification. Before seeing such parts in airplanes, adequate qualification and certification procedures must be laid out to ensure they perform as well as those made using traditional methods. It must be demonstrated that all manufactured parts reach the required standards in flame retardancy, mechanical behaviour and other aspects. When doing this, mechanical failure requirements such as tensile strength can only be verified through part destruction. As a result, the quality of parts for commercial use must be demonstrated to perform equally well as those tested by the manufacturer. In a method called First Article Inspection (FAI), the first parts produced are used as witness samples for mechanical testing while the remaining are sold to customers. Production requires consistent processing conditions to result in equally strong parts. Currently, such consistency with FFF is readily achievable only with expensive proprietary machines.

Open-source machines allow for customized materials but rely on the manufacturer to certify that parts meet the required standards. Their repeatability is not guaranteed, and any process deviations must be characterized and accounted for in the certification process. Since open-source machines are attractive in terms of cost and material freedom, there is an incentive for manufacturers to develop in-house solutions to guarantee their repeatability. This work will outline the requirements of such a solution and focus on the need for adequate process monitoring.

1.1 Project Goals

This project intends to build on preliminary qualification tests of filaments and printed coupons which laid the groundwork to evaluate the potential of open-source machines to produce aerospace-grade parts. Work is to be continued across multiple work packages to characterize the performance of filaments (off-the-shelf and custom) and open-source FFF machines.

The objective of this present work is to develop a framework to evaluate the consistency of processing conditions in open-source FFF via process monitoring. Methods to measure parameters affecting final part performance are to be identified and tested. Those showing potential to provide relevant data could then be implemented into a process monitoring apparatus.

1.2 Industry Needs

Currently, the only way to produce aerospace certified FFF parts is to acquire a pre-certified FFF machine and material such as the Stratasys Fortus 900 and Stratasys ULTEM 9085 (Figure 1.1). This system can produce aerospace-certified parts of outstanding quality. It also costs approximately $400,000 USD per machine and $517 USD per kg of filament. Another drawback of this system is that it is proprietary. This makes it difficult for users to gain an advantage over other users competing for the same clients. Companies want a solution with which they can leverage their research and development capabilities to offer quality parts at a competitive price.

(a)

(b)

Figure 1.1. The Stratasys Fortus 900 (a) [1] and Stratasys ULTEM 9085 (b) [2] are the current state-of-the-art proprietary solution for aerospace-grade FFF.

1.2.1 Reduce cost of printed parts

The primary goal of this project is to reduce the cost of industrial FFF parts. This step is crucial to make them competitive with established processes such as injection and compression moulding. The strategy adopted to reach this goal is threefold.

First, material cost needs to be reduced through part consolidation and vertical integration. The design flexibility of FFF enables the reduction of part count and fastener use. Cost can then be further reduced by purchasing generic filament and developing an in-house material qualification process. This would avoid the need for expensive aerospace-certified filaments.

Second, processing time and post-processing operations need to be reduced by optimizing printer settings. A systematic study of the influence of printing speed, raster width and height, and printing temperature will help determine the maximum deposition rate allowable without compromising part quality.

Third, the amount of required coupon testing for quality control needs to be reduced and replaced by real-time process monitoring. Process data should be gathered using an array of sensors and used as proxy for part quality. Such an apparatus could then be used to develop real-time process control with corrective capabilities.

1.2.2 Open-source 3D printing system

A major cost of FFF parts in the aerospace industry is the purchasing of proprietary materials and printing systems. This project aims to avoid this cost by developing an open-source process capable of producing aerospace-grade parts using generic materials. Open-source systems need to be reviewed and evaluated based on their potential to compete with the part quality of their proprietary counterparts.

1.2.3 Qualification process for printed parts

Upon procurement, generic materials are not certified for aerospace usage. There is a need to devise an in-house test plan to evaluate key parameters of newly bought materials. Such parameters include

- Fire, smoke, and toxicity properties,

- Dimensional tolerancing,
- Operating temperatures,
- Mechanical performance,
- Chemical composition,
- Surface finish, and
- Traceability of materials and processes.

Each parameter has its own requirements and measurement methods. This work will focus on mechanical performance, as it is heavily influenced by processing conditions and is currently a critical drawback of FFF relative to injection moulding and CNC machining. A procedure to evaluate the impact of processing conditions on mechanical performance is carried out in Chapter 6. As is good practice in academic and industrial research, the plan takes the form of a design of experiments (DoE). In the eventual context of industrial production, this plan would need to be adapted into a FAI procedure.

1.3 Technical Challenges

FFF provides a great amount of geometrical freedom but induces unique material properties which can vary depending on processing conditions. Print parameters need to be optimized for best possible result. Some parameters may have narrow processing windows, making thorough exploration of the design space challenging. This study aims to identify the most critical parameters and characterize their effect on mechanical properties. Results could then be used as starting points for future studies focusing on part optimization and certification.

There is also a challenge in wanting to make an open source FFF machine perform as well as a proprietary one. The model must be carefully selected to ensure its hardware has the potential to produce parts with desired repeatability. Open-source manufacturers often need to work around patent-protected features which could enhance print quality, speed, or reliability. This may include embedded sensors allowing printers to self-correct to minimize geometrical or thermal deviations. This project aims to develop an in-house data collection system to rigorously evaluate printer performance and ultimately serve as an indispensable certification tool. The industry has yet to develop certification standards for FFF parts and must resort to systematic mechanical testing. Proper sensing capabilities could dramatically reduce the amount of necessary testing and associated production costs.

1.4 Thesis Organization

This work begins in Chapter 2 with a review of the state of the art in process monitoring of FFF. It starts with a review of the literature focusing on mechanical test methods, material qualification processes, and strategies for monitoring and modelling. It follows with a review of the technology relevant to this project, including patents, printers, materials, laboratory equipment and thermal imaging cameras. Chapter 3 provides an overview of the process parameters studied in this work, as well as the Key Performance Indicators (KPI) used to evaluate process performance. Chapter 4 documents the work done to evaluate the default material and process parameters and determine which required additional tuning before formal characterization experiments could begin. In Chapter 5, the printing process is tuned to maximize quality and repeatability. This begins with the implementation of key improvements to the machine hardware and toolpath settings. The extruder flow rate and initial layer settings are then calibrated. Finally, a thermal monitoring method is developed at both low and high temperature to capture the thermal gradient of vertical tensile coupons. In Chapter 6, the effect of thermal gradient on weld strength is characterized using the developed monitoring method and a standard mechanical testing method. This work ends with concluding remarks and a proposal for future work to be carried out to better utilize process monitoring technology to allow cost-effective certification of FFF flying parts.

2 STATE OF THE ART

Toughness, formability, and reusability are few among the many reasons that make thermoplastic polymers the material of choice for FFF. This AM process has seen rapid growth in recent years with the development of high-performance machines (3D printers) and feedstock material (filament) [3]. With the aerospace industry now looking to produce non-critical structural components using this technology, reducing the notorious inconsistency in resulting mechanical properties is a pressing need. High-performance materials such as PEI and fibre-reinforced nylon exhibit promising strength and stiffness, but process-induced knockdown factors remain high [4]. To better understand the effect of process-induced features and defects, this chapter will survey the literature and technology landscape of FFF for the aerospace industry.

2.1 LITERATURE REVIEW

The impact of processing conditions on the mechanical behaviour of thermoplastic parts made with FFF is a growing topic of research thanks to the aerospace industry's increasing confidence in this technology. Although not standardized or specific to industrial FFF, several mechanical test methods for thermoplastic materials have been adapted to parts made with this process. Mechanical testing of printed coupons has provided data on material behaviour and the influence of print parameters on performance. These tests are the main component of current material qualification processes. However, process monitoring could reduce the amount of necessary testing and provide data to validate mathematical models of FFF. Data-driven models could enable real-time control as is done in other processes. Such a system could be integrated to a comprehensive process model or "digital twin" able to predict process performance without the need for physical testing. This section examines past work done in each of these areas.

2.1.1 Mechanical Test Methods

Properties are typically assessed through coupon testing following the guidelines of the American Society for Testing of Materials (ASTM).

Table 2.1 summarizes the mechanical test methods commonly used in FFF research. As seen in their titles, none of them are specifically formulated for FFF. In fact, standards specifically intended for testing FFF parts and comparing the effect of processing conditions do not yet exist. As such, researchers mostly rely on standards intended for classical polymer processing techniques.

Table 2.1. Mechanical Test Methods

Standard	Title	Properties of interest	Ref.
ASTM D638	Standard test method for tensile properties of plastics	Young's modulus, tensile strength, toughness, ductility	[5]
ASTM D790	Standard test method for flexural properties of unreinforced and reinforced plastics and electrical insulating materials	Young's modulus, flexural strength	[6]
ASTM D2344	Standard Test Method for Short-Beam Strength of Polymer Matrix Composite Materials and Their Laminates	Interlaminar strength	[7]
ASTM D5045	Standard Test Methods for Plane-Strain Fracture Toughness and Strain Energy Release Rate of Plastic Materials	Mode I fracture toughness, interlaminar strength, strain energy release rate	[8]

ASTM D638 is a versatile test method for tensile properties of plastics. The flat dogbone coupon geometry is readily manufactured using classical processes such as injection or compression moulding and CNC machining or cutting. Making them with FFF results in anisotropy, or orientation-dependent properties. As such, print orientation must be carefully selected. When conducting systematic testing for qualifying materials and processes, multiple orientations must be tested.

Ning et al. [9] used this test to measure the effect of print parameters on tensile performance. Samples were printed flat on the build plate varying five key parameters expected to affect mechanical performance:

- Raster angle: the angle of the printed bead relative to the x-axis. It is analogous to the fibre direction in a laminated composite.

- Feed rate: the speed at which the print head travels when laying down filament.
- Nozzle temperature: the temperature at which the filament exits the print head.
- Layer thickness: the effective height of the bead once laid down. It is controlled by incrementing the nozzle-bed distance by a fixed amount before each new layer.

Tensile testing provided data for measuring tensile strength, Young's modulus, toughness, ductility and yield strength of each specimen. It was found that a [0/90] raster angle exhibited significantly higher strength and stiffness than [±45], but lower toughness and ductility. Feed rate and nozzle temperature were both found to exhibit maximum strength and stiffness at an intermediate optimal setting. Thicker layers improved toughness and ductility abut resulted in voids if increased too much.

Fayazbakhsh et al. [10] used this test to evaluate the effect of manufacturing defects on tensile properties of PLA coupons printed flat on the build plate. Defects were simulated by intentionally skipping rasters during the printing process, leading to air gaps. It was found that air gaps transverse to the loading direction had a greater effect on tensile properties compared to longitudinal ones.

ASTM D790 is a flexural test method often used in conjunction with D638. Rectangular coupons are less slender and easier to print in all 3 directions. Chacón et al. [11] used both tensile and flexural test methods to study the effect of build orientation. Specimens were printed in 3 orientations relative to the print surface: flat, on-edge and upright (respectively X, Y and Z in Figure 2.1). Measuring tensile and flexural strengths, significant anisotropic behaviour was reported—build orientation was found to significantly impact mechanical properties, with ductility and failure profile varying the most. Upright samples were loaded parallel to the layer deposition direction and failed at the inter-layer fusion bond interface. Flat and on-edge specimens were loaded axially, and coupons carried significantly higher stress on the onset of failure.

ASTM D2344 is a short-beam test typically used to measure the interlaminar shear of polymer matrix composites. It consists of a 3-point bending setup where length-to-thickness ratio of the sample is about 4 to induce shear rather than bending. This simple apparatus makes it a popular tool to evaluate the impact of process conditions during research and development or quality control. It is readily adaptable to FFF coupons which have a similar laminated structure with oriented properties. Berretta et al. [12] used this approach to measure the inter-layer bond strength of coupons made with custom PEEK filament.

ASTM D5045 is a compact tension test designed to measure the fracture resistance of polymers. It can be adapted to FFF by testing coupons printed flat and upright to account for orthotropy. Arif et al. [13] studied the fracture mechanics of 3D printed PEEK. Compact tension specimens were printed at different orientations (flat and upright) and raster angles (0° and 90°). Upright samples were identified as prone to delamination. The failure observed was described as stick-slip fracture. Interfacial voids prevented cracks from propagating continuously, causing both initiation and termination. The cause for such porosity was attributed to insufficient cooldown time between the printed layers. As a remedy, the authors proposed minimizing thermal gradients across beads to maximize macroscopic properties, while recognizing this would involve increasing overall print times and decreasing productivity.

Aliheidari et al. [14] analyzed the fracture resistance and inter-layer adhesion of ABS specimens. In a method similar but not identical to ASTM D5054, double cantilever beams (DCB) were printed at different nozzle temperatures to obtain different amounts of inter-layer fusion. Specimens were loaded in a crack-opening mode. Inter-layer adhesion strength was calculated based on the load on the onset of crack growth. Specimens printed at a higher nozzle temperature exhibited significantly higher strength, while modulus remained relatively constant.

As seen from these studies, mechanical testing of FFF coupons is done by adapting existing methods intended for plastics or composites. Although these have provided useful data to understand the process-induced properties of FFF parts, there is a need to develop specific methods that systematically capture these intricacies. According to the Composite Materials Handbook committee (CMH-17), there is insufficient test data to inform standard testing procedures specific to FFF as of November 2021. Sampling strategies and equivalency calculations are not currently defined for polymer AM. Working groups at CMH-17 are currently investigating sources of variation in the materials and processes to implement a multivariate regression approach for statistical analysis of test samples [15]. The group notably intends to solve the printability issues found in ASTM D638: slender dogbone coupons can oscillate when printed vertically, resulting in increasing defects along the build direction. Industrial and academic partners of CMH-17 are currently investigating alternative test specimens addressing this shortcoming. Leading candidates in terms of printability include a reduced length version of ASTM D638 and Boeing's double flare sub-scale specimen.

2.1.2 Material Qualification Processes

Mechanical test data is useful for defining design guidelines and essential for part qualification. This process is a requirement for certifying parts for use in aerospace. Mechanical testing is lengthy and expensive. To produce aerospace-grade FFF parts, aerospace companies may also opt for a turnkey solution like the flagship Fortus 900 system sold by Stratasys. This state-of-the-art machine uses proprietary filament feedstock which comes pre-certified for aerospace use. The cost of ownership for such a system is often prohibitive. To reduce costs and access cheaper open-source materials, industrial players may opt to use it as a benchmark for qualifying generic materials. This initiative is enabled in part by National Center for Advanced Materials Performance (NCAMP). This organization has compiled a set of qualification methodologies and database of test results for the Stratasys ULTEM 9085. Specific documents are listed in Table 2.2.

Manufacturers may use this information to perform equivalency testing to qualify the performance of open-source machines and materials. Referring to section 8.4.1 of CMH-17-IG, a filament can be qualified like the proprietary one if it passes the same tests. A sample test plan is outlined below based on NCAMP documents and past work.

Table 2.2. Stratasys ULTEM 9085 NCAMP Documentation

Code	Title	Page count	Description	Ref.
NPS 89085	Process Specification	43	States how to make test coupons with a Stratasys F900 and which coupon tests to perform.	[16]
NMS 085	Material Base Specification	15	States which filament tests to perform.	[17]
NMS 085/1	Material Slash Specification	7	Provides the requirements for printed coupon test results.	[18]
CAM-RP-2018-013	Material Property Data Report	406	Provides references for equivalency testing and fixture design, as well as test data.	[19]
NCP-RP-2018-007	Statistical Analysis Report	126	Explains which statistical tools to use and provides details for each test performed.	[20]

2.1.2.1 Incoming material

Batches of filament arrive from a commercial supplier or in-house production. Suppliers issue a certificate of performance, but more qualification is required to satisfy the demands of the aerospace industry. A label is applied to maintain internal traceability.

2.1.2.2 Filament Analysis

Filament properties must be verified to ensure clean and dimensionally accurate extrusion. These tests are summarized in Table 2.3. Filament spools which pass them can then be used for coupon manufacturing.

A critical property of any polymer used in FFF is its glass transition temperature (T_g). It is the temperature above which chains begin to slide against one another. NCAMP prescribes T_g measurement using differential scanning calorimetry (DSC) following ASTM E1356. To comply with NCAMP criteria, the T_g of ULTEM 9085 must fall between 177.9°C and 183.1°C.

Characterizing melt flow is also important to consistent extrusion during printing. The standard test for melt flow characterization is ASTM D1238 and uses an extrusion plastometer. Over a 10-minute period, 6.5 to 11.0 g of melt must flow to satisfy NCAMP criteria. Using a rheometer to measure melt properties such as viscosity, storage and loss moduli, and overall stress relaxation behaviour may also provide useful insight into material behaviour for modelling purposes but isn't prescribed by NCAMP.

Moisture content in filament must be tightly controlled to avoid significant knockdown in properties. Upon reception, the filament must be dried in an oven and stored in a sealed dry cabinet. Its relative moisture content is monitored periodically using a moisture analyzer following ASTM D7191-18. Prior to printing, it must not be above 0.04%.

Extruders in FFF machines are sensitive to variations in filament diameter. Significant deviation or ovality can cause slippage with the driving gears, resulting in filament under-extrusion. Filament diameter and ovality should be closely monitored using a laser micrometer along its entire length. This should be done preferably during printing to avoid having to rewind the spool. The diameter should always fall between 1.715 and 1.877 mm with an average of 1.75±1 mm. Ovality, or difference between major and minor diameter, must never surpass 0.071 mm.

Table 2.3. Filament Tests Prescribed by NCAMP

Standard	Title	Min.	Max.	Ref.
ASTM E1356-08	Standard Test Method for Assignment of the Glass Transition Temperatures by Differential Scanning Calorimetry	177.9°C	183.1°C	[21]
ASTM D7191-18	Standard Test Method for Determination of Moisture in Plastics by Relative Humidity Sensor	-	0.04%	[22]
ASTM D1238	Standard Test Method for Melt Flow Rates of Thermoplastics by Extrusion Plastometer	6.5 g/10min	11.0 g/10min	[23]
N/A	Diameter Measurement by Laser Micrometer	1.715 mm	1.877 mm	[17]
N/A	Ovality Measurement by Laser Micrometer	-	0.071 mm	[17]

2.1.2.3 Coupon analysis

Coupon analysis is comprised of physical and mechanical testing. Both serve as tools to evaluate the influence of the printing process on neat mechanical properties. The tests to perform are summarized in Table 2.4 and Table 2.5.

Physical tests are used to evaluate the repeatability of the machine and the quantity of defects it induces. Thickness is measured using a micrometer at three different points in the gauge region of the tensile samples. The average measurement must fall between 2.977 and 3.561 mm. Density is calculated by weighing samples in air and submerged in water following ASTM D792-13. The resulting value is the density of the sample itself, accounting for the material itself plus any internal air gaps or voids. Characterizing the coefficient of thermal expansion is done by printing samples for thermo-mechanical analysis (TMA) following ASTM E831-05. The glass transition temperature is characterized once again, this time by dynamic mechanical analysis (DMA) following ASTM D7028-07.

Table 2.4. Coupon Physical Tests Prescribed by NCAMP

Standard	Title	Min.	Max.	Ref.
ASTM D3171-15	Standard Test Methods for Constituent Content of Composite Materials (used to measure thickness)	2.977 mm	3.561 mm	[18]
ASTM D792-13	Standard Test Methods for Density and Specific Gravity (Relative Density) of Plastics by Displacement	-	-	[19]
ASTM E831-05	Standard Test Method for Linear Thermal Expansion of Solid Materials by Thermomechanical Analysis	-	-	[24]
ASTM D7028-07 (wet and dry)	Standard Test Method for Glass Transition Temperature of Polymer Matrix Composites by Dynamic Mechanical Analysis	-	-	[25]

Mechanical test coupons must be manufactured to evaluate the performance of the as-printed material. NCAMP prescribes four print orientations per print: X, Y, Z, and Z45 (see Figure 2.1). The impact of temperature and moisture are evaluated by conducting mechanical tests in five different environmental conditions: cold temperature dry (CTD, -54°C), room temperature dry (RTD, 21°C), room temperature wet (RTW), elevated temperature dry (ETD, 82°C), and elevated temperature wet (ETW). The impact of build location must also be accounted for. Specimens should be printed in the centre, top and bottom left, and top and bottom right of the build plate. The analysis of variance (ANOVA) method is used to determine which parameters influence the resulting properties. Those that do not significantly affect them may then be grouped together to reduce the required number of coupons. The mean, coefficient of variation and B-basis values are reported.

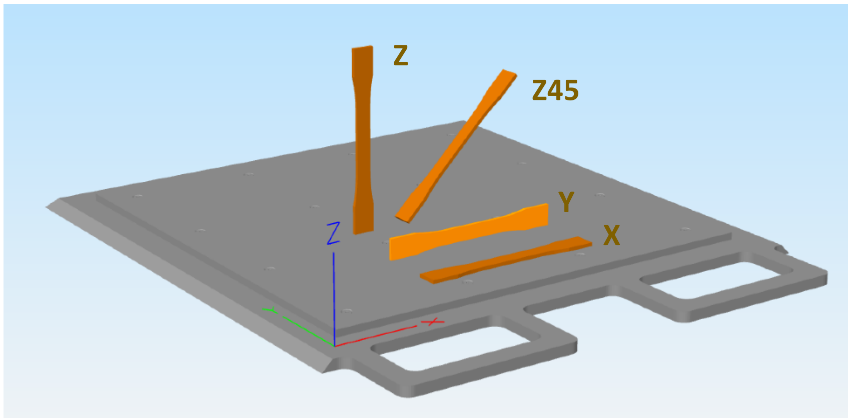

Figure 2.1. Print orientations prescribed by NCAMP (adapted from Clarkson et al. [20]).

Table 2.5. Mechanical Tests Prescribed by NCAMP

Standard	Type	Properties of interest	Ref.
ASTM D638	Tension	Modulus, UTS, EAB, Poisson, Yield	[5]
ASTM D790	Flexure	Modulus, UFS	[6]
ASTM D695	Compression	UCS, Yield	[26]
ASTM D5379	V-notch shear	Modulus, UTS	[27]
ASTM D256	Izod impact	Impact resistance	[28]
ASTM D5766	Open-hole tension	Modulus, UTS	[29]
ASTM D6742	Filled-hole tension and compression	Modulus, UTS	[30]
ASTM D6484	Open-hole compression	Modulus, UCS	[31]
ASTM D5961	Single shear bearing	UTS, Deformation	[32]

2.1.2.4 Outgoing material

After in-house qualification, the material is ready for aerospace-grade production. NCAMP specifies that no external process monitoring apparatus is necessary when using Stratasys systems. However, it is recommended when using open-source systems.

2.1.3 Process monitoring strategies

Systematic refinement of the printing process can strongly benefit from live data collection. Process monitoring can be used to detect printing issues early and call for process termination or corrective actions. Aggregating data from multiple sensors can detect defects which no single sensor could reliably do. Moretti et al. used positional encoders to measure motor accuracies and localize nozzle temperature readings in space and time [33]. Thermocouples were mounted both in the nozzle and the hot end. The combined data revealed temperature spikes associated with initial layer defects. Compton et al. used a FLIR A35 thermal camera to measure the interlayer temperature gradient of printed thin walls [34]. Data was used to validate a 1D finite difference model for transient heat transfer. Wang et al. also used a FLIR camera to measure temperature gradients of printed parts [35]. This time, data was used to build a linear regression model for predicting layer temperature. Pooladvand and Furlong [36, 37] used a camera to validate an 3D discretized thermal model. Thermal gradients were measured by mounting a thermal camera just outside the printer. Kousiatza and Karalekas [38] embedded thermocouples and fibre optic sensors within samples during the printing process. Thermocouples revealed oscillating temperature profiles with repeating nozzle passes. Fibre optic sensors enabled the measurement of free-standing residual strain at room temperature. Tlegenov et al. [39] developed an analytical model of the forces in the extrusion process. This model was used to detect clogging by monitoring the electric current drawn by the extruder stepper motor. Preissler et al. [40] used a stereoscopic camera and fringe projector to measure the geometrical variations of printed layers. A point cloud was generated for each layer and compared to the G-code input to identify deviation. A summary of sensor uses for in-situ process monitoring in FFF is provided in Table 2.6.

Some sensors are not well suited for in-situ data acquisition due to bulkiness or need for controlled environment but can still help understand the effect of different process conditions. Levy [41] used a rheometer to characterise the viscosity and stress relaxation of laser-welded ABS. The data was used to develop a solidification model to determine optimal solidification time. De Pretto et al. [42] used optical coherence tomography (OCT) to identify poor bonding and dimensional deviations in PLA made with FFF. A summary of sensor uses for post-process evaluation of FFF parts is provided in Table 2.7.

Table 2.6. Sensors for In-Situ FFF Process Monitoring

Sensor	Purpose	Ref.
Positional encoder	Measure motor accuracy Localize data within the build space	[33]
Thermocouple	Measure temperature of nozzle, hot end, build plate, enclosure, and part	[33, 38]
Optical camera	Evaluate layer quality	[33]
Thermal camera	Measure layer temperature and thermal gradient	[34, 35, 43, 44]
Fibre optic sensor	Monitor internal stress of part	[38]
Current sensor	Detect nozzle clogging	[39]
Stereoscopic camera	Measure layer roughness	[40]

Table 2.7. Sensors for FFF Post-Process Evaluation

Sensor	Purpose	Ref.
Microscope	Surface roughness	[45]
Hygrometer	Moisture content	[43]
Micro-CT	Porosity	[43]
Rheometer	Melt viscosity and stress relaxation behaviour	[41, 43]
Optical coherence tomography	Evaluate bonding and dimensional accuracy	[42]

Image analysis is often used in conjunction with mechanical testing. Beretta et al. [12] investigated material surface and fracture profile using scanning electron microscopy (SEM). Micro computer tomography (Micro-CT) was used to measure the porosity of the printed parts.

Riddick et al. [46] used fractographic analysis to study the relationship between the mechanical properties and failure mode. SEM was conducted on the fracture surface of tensile specimens. Fractographic analysis revealed that specimens printed on-edge had the least inter-bead voids, resulting in higher strength. Upright samples were the weakest. The [±45] raster angle was found to partially strengthen them through a proposed toughening effect.

Mechanical tests and process monitoring are powerful tools to build an empirical understanding of the mechanical behaviour of polymer structures made with FFF. However, to derive constitutive models that accurately predict their response, a molecular-level understanding is required.

2.1.4 Process modelling

Process modelling is a powerful tool to predict residual stress and warpage, two common causes of print failure. Models take part geometry and processing conditions as inputs and carry out a series of physics-based computations. FFF is a highly coupled multi-physical process. Mathematical models must be drawn from the fields of fluid flow, heat transfer, and solid mechanics. The process is typically decomposed into three steps to be analyzed individually: (1) polymer melt flow, (2) deposition and bond formation, and (3) solidification and residual stress. A literature review by Brenken [47] provides a list of papers attempting to model each of these steps.

2.1.4.1 Polymer Melt Flow

Modelling the flow of molten filament through the hot-end and out the nozzle can provide insight into the effect of different extrusion parameters on the printed bead. Bellini [48], Ramanath [49], and Nikzad [50] developed models for velocity, pressure, and temperature of neat Newtonian melts. Nixon [51], Garcia [52], Heller [53], and Lewicki [54] incorporated the flow of chopped fibres as rigid bars within the polymer melt. All found that fibres tend to align with the direction of flow in areas of high shear.

Most attempts to model melt flow during extrusion assumed it to be Newtonian and isotropic. However, with the addition of fibre reinforcements, this assumption no longer holds true. Melt flow causes fibre alignment which in turn makes its viscosity anisotropic [47]. Accurate process modelling therefore demands a coupled relationship between viscosity and fibre orientation.

2.1.4.2 Deposition and Bond Formation

Bead deposition and adhesion to the layer underneath it is critical for structural integrity of printed parts. Inappropriate parameters can cause significant knockdown in mechanical properties and geometrical accuracy. Thomas [55] developed a 2D analytical heat transfer model coupled with molecular reptation theory to predict the fracture strength between two beads based on their thermal history. Free convective boundary conditions and negligible contact resistance were assumed. The initial wetting stage was identified as most critical to get strength, as well as a low cooling rate. Li [56] used a one-dimensional lumped capacitance analysis (LCA) coupled with necking kinetics to quantify the weakening due to incomplete bonding of adjacent beads. Sun's 1D LCA model [57] captured the effect of air and nozzle temperatures on bond thermal history and strength, again indicating that low cooling rates are desirable to maximize strength.

FFF is a highly unsteady process with an expanding domain, phase change and evolving thermal gradient. By establishing the print head as the frame of reference, Yardimci [58] was able to develop a 2D quasi-steady-state heat transfer model. Costa [59] used "stepwise activation" to capture the transient nature of FFF by expanding the domain of analysis at each time step. This concept was used in more recent 2D and 3D finite element models by Brenken [60] and Zhou [61].

It was shown by Ravi et al. [62] that laser pre-heating was an effective method for inter-layer bond strengthening. However, current physics-based models of bead coalescence do not yet capture the effect of fibre reinforcements. In fact, fibres may affect melt surface tension and promote crystal nucleation.

A physical phenomenon critical to the process of interlayer bonding is thermoplastic healing. Wool and O'Connor [63] proposed a model where a healed crack recovers a fraction of its mechanical properties as a function time, temperature and pressure. Upon contact, molecules diffuse and randomize between surfaces, resulting in progressive crack healing. This concept has been applied to thermoplastic composite manufacturing processes such as compression moulding. Bastien and Gillespie [64] specifically focused the AS4/PEEK composition when developing their model. Again, time and temperature dictate the degree to which molecules diffuse across surfaces in intimate contact.

2.1.4.3 Bead Solidification and Residual Stress

The rate of solidification of the printed layer over time dictates the amount of residual stress developed in the structure. Wang [65] derived an analytical solution for the elastic behaviour of FFF parts. Stress buildup was assumed to begin when the layer temperature dropped below its T_g. The model also assumed instant layer deposition, resulting in purely vertical thermal gradients. Zhang [66] used stepwise activation to obtain a 3D thermal gradient which could be qualitatively compared to experiments. Print speed was found to have the highest impact on the gradient. Hébert [67] developed a warpage model where coefficient of thermal expansion (CTE) and elastic modulus were functions of temperature. Talagani [68] also used stepwise activation of a 3D mesh generated from G code. Residual stress and warpage results were used in a fracture mechanics model to predict the failure at the bead interface. Brenken [69] considered both crystallization and CTE as sources of residual stress and warpage. A 3D finite element model was used to obtain solutions for temperature, crystallinity, stress, and displacement. Warpage was predicted by releasing boundary conditions and validated through benchmark experiments. Thermomechanical models of the FFF process implement thermal contraction to predict residual stress and deformation. Brenken et al. [47] note that melt viscoelasticity has not yet been considered in published literature. This must be implemented to capture effects such as sagging at high temperature.

2.1.5 Real-time process control

3D printers are complex multi-physical systems which require some degree of active control to work properly. Machines make use of open and closed-loop control to ensure settings remain with their allowable range and result in optimal print performance. This section examines the control strategies used in printer subsystems and avenues of improvement to increase reliability and ultimately reduce the required amount of witness coupon testing.

2.1.5.1 Thermal control

A fundamental requirement of an FFF printer is a closed-loop temperature-controlled nozzle. This is essential for consistent filament extrusion whose viscosity is highly temperature dependent. Many conventional machines also have actively heated beds to promote first layer adhesion and some even control the temperature of the chamber. This feature minimises thermal contraction during printing and is essential for high temperature filaments such as PEI. Thermal control is typically achieved through a proportional-integral-derivative (PID) strategy optimised for a specific target temperature.

2.1.5.2 Motion control

Axis motion is typically under open-loop control. It may be controlled by highly accurate stepper motors, but the use of positional encoders or accelerometers to compensate for vibration, hysteresis, or other forms of deviation is still rare. Of the open-source systems reviewed, none make use of such sensors. Moretti et al. [33] retrofitted positional encoders to a custom-built printer, but did not use the data for corrective purposes (this was stated as a future application).

Despite open-loop control, motor accuracy can be increased by modifying its kinematics. A typical velocity curve for a 3D printer stepper motor is trapezoidal. The velocity increases linearly up to the set print speed and then decreases linearly so that it is zero at the endpoint. Yu et al. [70] noted a critical flaw of the trapezoidal curve: in between each step, motor torque must change quasi-instantly (Figure 2.2). This results in high jerk (rate of change of acceleration) which can compromise print quality. The researchers examined the performance of a five-phase S-curve as an alternative where acceleration varies linearly instead of velocity. This solution allows the jerk to be controlled and kept to a minimum, resulting in increased surface quality.

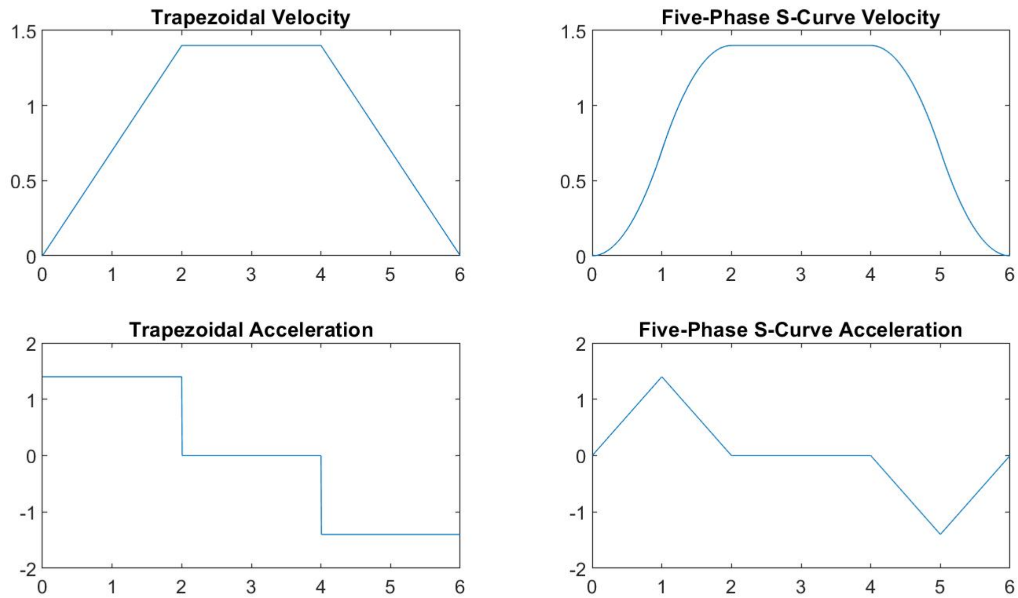

Figure 2.2. Kinematics of trapezoidal and five-phase S-curve motor motion profiles (adapted from Yu et al. [70]).

2.1.5.3 Active feedback

Active feedback (or closed-loop control) for non-thermal parameters has been implemented in customized FFF solutions to increase quality and reliability. Cheng et al. [71] devised a process control system for FFF based on visual inspection feedback. Voids and overfills were detected through image analysis, comparing layer images to the geometry specified in CAD. Raster shape was inferred based on image shading. Random defects were detected by comparing image pixels to those of a synthetic defect-free image. Filament deposition rate was then modulated when printing the next layer to compensate for these defects.

Combining process monitoring and predictive modelling strategies can ultimately be used to implement real-time process control. This was achieved by Wang et al. [35] using a linear regression model generated from thermal data. The model was used to predict the cooldown rate of printed layers and ensure the layer being printed on was within the right temperature range to promote adhesion and minimize deformation. Model predictions were used to maximize the deposition rate while maintaining a suitable thermal gradient.

2.1.6 Digital twins

The result of thoroughly integrated process monitoring, simulation and control is known as a digital twin or virtual replica of the industrial system. It combines high-fidelity process models with data collection to provide insight on the system's life cycle. A digital twin is different from conventional engineering simulation in that it provides a comprehensive understanding of the behaviour of the system. Data and models are used in conjunction to predict and optimize performance [72]. Elements of digital twins include the following:

- Sensors for acquiring data from the physical system during testing and operation.
- Digital thread, or pipeline of information fed back from sensor to models.
- Edge (i.e., local) computers to process sensor data, run mathematical models, provide maintenance warnings, and dynamically adapt the system to its environment.
- Cloud computers to aggregate data from fleets of systems to increase learning capability.
- Graphical user interfaces to convey technical information or to artistically illustrate the system in action. This may include the display of CAD models through virtual or augmented reality [73].

Digital twins benefit massively from machine learning and parallel computing. Traditional finite element (FE) methods solved using commercial codes have been shown to yield accurate physics-based solutions at the cost of high computing times. However, detailed 3D FE models of multi-physics processes are too slow for real-time processing. A promising alternative for time saving is the use of neural networks. Algorithms built from these are purely data driven (i.e., the underlying equations do not capture the physics at play). As such, they require large training datasets which can be readily collected in traditional high-volume manufacturing thanks to modern sensor technology. In the low volumes typically associated with AM and aerospace manufacturing, such datasets may not be available. As an alternative, Zobeiry and Poursartip [74] generated training data using finite element models in a paradigm called theory-guided machine learning (TGML). TGML incorporates physics into traditional machine learning, resulting in accurate solutions obtained in times considerably lower than with FEA.

2.1.7 Part design considerations

Designing parts for FFF must consider the material directionality induced by the process. As such, there is an opportunity to learn from the field of polymer composites and borrow design techniques capturing the effect of anisotropy. For example, Ahn et al. [75] treated raster angle as fibre orientation to apply classical laminate theory to FFF samples. The applicability of the Tsai-Wu failure criterion has also been investigated. Recent advances in the composites field may also be useful for FFF part design. The double-double (DD) method developed by Tsai [76] may be an effective tool to determine optimal raster angle. However, such considerations are outside the scope of this work which will concentrate on process monitoring strategies.

2.2 Technology Review

Developing a tightly controlled 3D printing process requires an array of sensors to monitor printing parameters in real time. Data collected during production could replace expensive sample testing for quality control, streamlining the process significantly.

2.2.1 Patents

The foundational patent for FFF is "Apparatus and Methods for Creating Three-Dimensional Objects" by Crump of Stratasys in 1992 [77]. It describes a mobile head dispensing molten material while moving in three dimensions via computer numerical control. Since the patent's expiry in 2012, the technology has become increasingly accessible with new open-source solutions being released every year.

Commercial FFF of high-temperature thermoplastics is a relatively new market where industry players develop machines with increasing size, performance, and efficiency. Stratasys was the first to step in, patenting its "High Temperature Modelling Apparatus" in 2004 [78]. A key feature of this invention is the "deformable thermal insulator" or bellows shielding the extruder from the heated enclosure (Figure 2.3). This feature is still found today in the Fortus 900, the company's flagship product [79].

Figure 2.3. Low angle shot of a Stratasys Fortus 450mc chamber showing the bellows shielding the extruder from the heated enclosure.

2.2.2 FFF Printers

Competitors have had to develop alternatives to such patented features to commercialize their own solutions. Montreal company AON3D have integrated the gantry into the heated chamber and make use of a liquid cooling system to protect the motors and extruder. Their M2 system has a build volume larger than most reviewed high-temperature printers, at 395 x 420 x 640 mm. The latest high-temperature open-source system to be released is the 3DXTECH Gearbox HT2. It features similar specifications to the M2. Table 2.8 compares the main specifications of the two printers beside those of the Stratasys F900 used as qualification benchmark in this project.

Table 2.8 Comparison of Industrial FFF Machines

		AON3D M2	**3DXTECH Gearbox HT2**	**Stratasys F900**
Build volume [mm]		395 x 420 x 640	457 x 457 x 813	914 x 610 x 914
Layer height [mm]		0.05 - 0.5	Unknown	Unknown
Nozzle width [mm]		0.2 - 1.2	0.25 – 1.0	Unknown
Resolution [mm]	XY	±0.025	±0.127	±0.089
	Z	±0.001	Unknown	±0.089
Temperature [°C]	Nozzle	470	500	Unknown
	Bed	200	225	Unknown
	Enclosure	135	225	Unknown
Connectivity		WIFI, Ethernet	Unknown	MTConnect
Materials	Capacity	PEEK, PEI	PEEK, PEI	PEEK, PEI
	Freedom	Open	Open	Closed
Machine cost [USD]		60,000	182,000	400,000

2.2.3 Materials

Thermoplastic materials used in FFF typically fall into one of three categories forming the so-called "pyramid of thermoplastics" [80]. At the bottom are commodity polymers found in consumer-grade FFF such as poly-lactic acid (PLA) and acrylonitrile butadiene styrene (ABS). In the middle are engineering polymers such as polycarbonate (PC) and polyamide (PA, nylon) which feature higher durability and strength. At the top are high performance polymers such as poly-ether-ether-ketone (PEEK) and poly-ether-imide (PEI). These materials combine superior mechanical properties with heat resistance. Aerospace manufacturing is typically restricted to this category due to flame, smoke, and toxicity (FST) requirements.

ULTEM 9085 is a polymer blend combining PEI and PC at about 80%/20% by weight. This staple of aerospace manufacturing is also the material used in NCAMP's certification procedure for the Stratasys F900. Unlike PEEK, it is amorphous (i.e., polymer chains cannot pack to form crystals). Like many high-end polymers, it readily absorbs moisture from the air which can significantly impact its printability and mechanical properties.

2.2.4 Laboratory Equipment

Handling, storage, and processing of high-performance polymers such as PEI requires careful control of environmental conditions. In a past project carried out by the industrial partner, Tao [81] selected a series of equipment and sensors for filament quality control. These items are listed in Table 2.9.

2.2.5 Thermal Imaging Cameras

As seen in the review of process monitoring strategies (Section 2.1.3), thermal imaging (aka. infrared thermography) is a powerful tool to evaluate the bond quality between layers. To incorporate such measurements into this work, four different cameras were reviewed based on the recommendations of a supplier. Their specifications are summarized in Table 2.10. The FLIR A70 and Fluke RSE300 are intended for scientific research while the FLIR T420 and Fluke TV46 are designed for commercial use. The T420 is a portable handheld model while others are screw mounted. The TV46 can withstand temperatures of up to 140°C thanks to an external water-cooled enclosure (sold separately, included in cost estimate). The FLIR Thermal Studio software is intended to quickly generate thermal reports in PDF format using customizable templates. The Fluke ThermoView software is more geared towards direct analysis. It is also compatible with MATLAB and LabVIEW for enhanced functionality. Camera selection was made based on availability, cost, and resolution. The T420 already acquired by the industrial partner was chosen for immediate use while the A70 was purchased by McGill for future experiments.

Table 2.9. Laboratory Equipment for Filament Quality Control

Type	Name	Purpose
Dry cabinet	Dr. Storage X2B	Store filament spools below 5% rh.
Moisture analyzer	Brookfield Ametek Computrac Vapor PRO XL	Measure the relative moisture content of filament samples cut from spools following ASTM D7191.
Temperature and humidity sensor	Omega ITHX-SD	Measure the temperature and relative humidity of the room.
Laser micrometer	Laserlinc Triton 312	Measure the diameter and ovality of the filament along the entire length of the spool.

Table 2.10. Comparison of Thermal Imaging Cameras

	FLIR A70	FLIR T420	Fluke RSE300	Fluke TV46
Frame size (px)	640 x 480	320 x 240	320 x 240	640 x 480
Min. focus distance (mm)	200 (fixed)	400	150	152
FOV (°)	51 x 39	25 x 19	34 x 24	34 x 25.5
Resolution at min. focus distance (mm/px)	0.39 x 0.34	0.58 x 0.57	0.32 x 0.28	0.16 x 0.15
Software	FLIR Thermal Studio (subscription)		Fluke ThermoView (one-time purchase)	
Max. operating temperature (°C)	50	50	50	140
Est. cost (CAD)	13,500	25,000	15,000	43,000

2.3 SUMMARY

This review of the literature and technology yields the following conclusions.

- The mechanical test methods required for certifying the properties of printed parts have been widely studied by adapting existing procedures intended for plastics and polymer matrix composites.
- NCAMP's state of the art test plan is sufficient to certify the performance of a closed Stratasys machine but has yet to be formally adapted to open-source systems.
- The ASTM D638 tensile coupon presents some printability issues but remains the geometry of choice for evaluating the impact of process conditions on mechanical properties.
- Printing coupons in the Z-direction will highlight the inter-layer bond strength and stiffness.
- Process monitoring can provide valuable data to evaluate and improve part quality. Of all the sensors surveyed, the thermal imaging camera was the most popular for in-situ monitoring. It can provide a full field reading of the print's thermal profile, gradient, and cooldown rate.
- Infrared (IR) thermography can be used to validate heat transfer models and evaluate the repeatability of the printing process.
- Deviation feedback based on data or physics-driven models could become powerful tools for part qualification. However, this applicability has yet to be demonstrated.
- The AON3D M2 is an attractive platform for high-temperature FFF research due to its low cost and open material selection.
- ULTEM 9085 is a natural choice for coupon printing to allow comparison of results with those of NCAMP.
- Exposure to humidity can significantly deteriorate printability and mechanical properties of ULTEM 9085. A tightly controlled environmental conditioning procedure must be laid out and followed to ensure that moisture is not a source of variability.

2.4 Research Objectives

In line with the goal of developing a framework to evaluate the consistency of processing conditions in open-source FFF via process monitoring, thermal imaging is identified as a promising solution to measure parameters affecting final part performance. The primary objective of this thesis is to utilize this technology to record the full-field thermal profile of printed parts in-situ to gain insight into layer healing and solidification. Before this can be achieved, the following sub-objectives must be satisfied.

2.4.1 Parameter Identification

Since the thermal profile of printed parts cannot be directly controlled, process parameters which impact it must be identified. Intentionally varying those parameters should result in measurable variations in thermal profile while staying within the material processing window. This will enable the printing of geometrically identical coupons with different thermal histories.

2.4.2 Process Evaluation and Tuning

Before carrying out experiments, the default print settings must be tuned to provide consistent baseline quality and reliability. Default settings will be evaluated by printing benchmark geometries and sample coupons. Hardware improvements should also be carried out at this point. The final step of this stage is to develop a thermal monitoring method to be used during experiments.

2.4.3 Design of Experiments

Ultimately, a DoE is to be devised where the thermal profile is varied between runs and resulting mechanical properties are tested using ASTM D638. The effect of thermal history on tensile strength and modulus can thus be determined. The resulting data could then be used to validate process models developed in future work.

3 CONTEXT AND METHODOLOGY

This section introduces the FFF process and provides an overview of aspects relevant to this project. Specific process parameters are listed along with their expected impact on resulting part properties, hypothesised according to underlying physical principles. Key concepts and print features are illustrated using schematics and samples printed for this purpose. Metrics are also proposed to measure the impact of these parameters.

3.1 PROCESS OVERVIEW

At its core, FFF consists of a nozzle extruding thermoplastic filament in a highly controlled manner. Material is deposited onto a build plate in the form of a bead (or raster). Juxtaposed beads form layers which successively stack on top of one another. The initial layer adheres directly to the build plate (Figure 3.1a) while subsequent layers bond to the one below them. The thicknesses of each layer add up, giving the final part its height (Figure 3.1b).

(a)

(b)

Figure 3.1. Photographs of FFF process using carbon fibre-reinforced nylon filament showing initial printed beads (a) and finished parts (b).

The extruder is mounted on a gantry allowing it to move parallel to the build plate (or bed) in the X and Y axes. Perpendicular motion in the Z axis is achieved either by lifting the gantry or lowering the build plate. In the AON3D M2, the latter configuration is used (Figure 3.2).

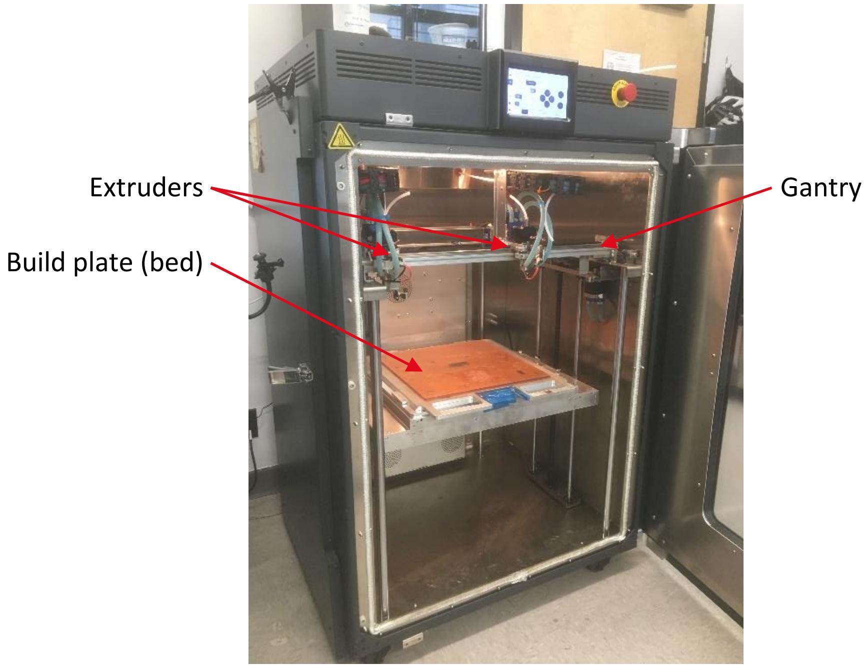

Figure 3.2. Photograph of the AON3D M2 chamber showing extruders, gantry and build plate.

Material is supplied by a spool of filament. In the AON3D M2, spools are held at the back of the machine and fed inside via a PTFE tube. The tube feeds directly into the extruder. The extruder gears grip the filament and push it through the hot end and nozzle which respectively melt and extrude it (Figure 3.3).

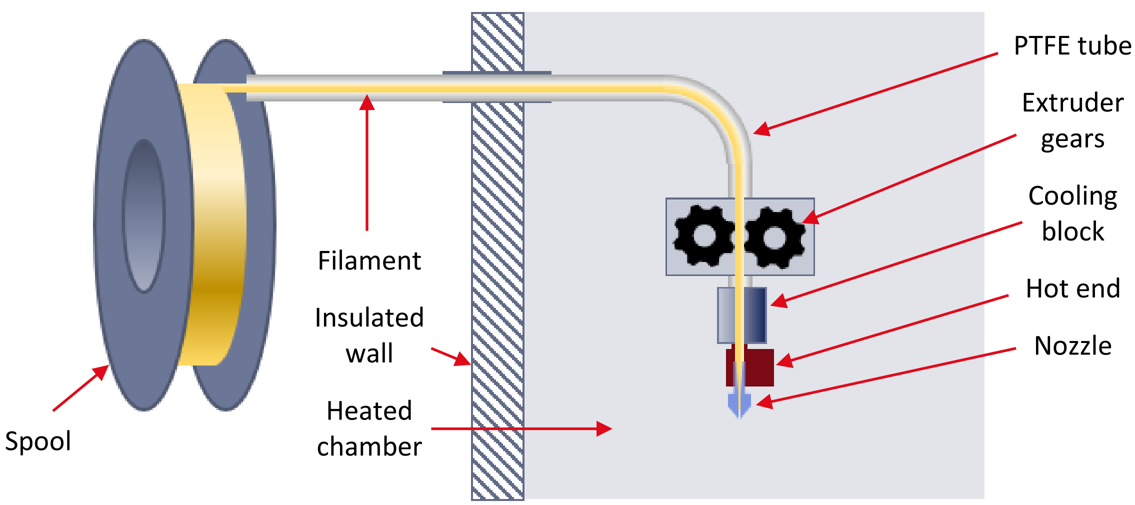

Figure 3.3. Schematic of the material feeding process in the AON3D M2.

This process is largely automated by the machine's embedded electronics. The amount of control given to the user depends on the machine and software used. As an open-material industrial printer, the AON3D M2 allows more user input than proprietary systems but not as much as custom-built ones. For example, the PID constants for thermal control can be edited in the machine terminal, but the flowrate of liquid coolant cannot be changed. The following section discusses parameters which can be controlled and optimized for best performance.

3.2 Process Parameters

Process parameters (also called print settings or profiles) are defined by the user in the slicing software (or slicer) and fed to the printer via G code. Slicers such as Ultimaker Cura [82] and Simplify3D [83] offer customizable settings to achieve desired print quality. The following settings were selected as relevant to understanding the FFF process and the scope of this work. Process parameters are typically tuned via trial-and-error or DoE. Once optimal parameters have been defined for a given material, machine, and part, they can be saved for future use as a standard operational procedure (SOP).

3.2.1 Adhesion parameters

Initial layer adhesion is often regarded as the most crucial step for a successful 3D print. Adequate bonding to the build plate ensures the part is firmly held in place during the rest of the print. Since most printers cannot track the position of the part being printed, an unstable print will almost always result in print failure. To mitigate this, key adhesion settings (Figure 3.4) must be properly tuned.

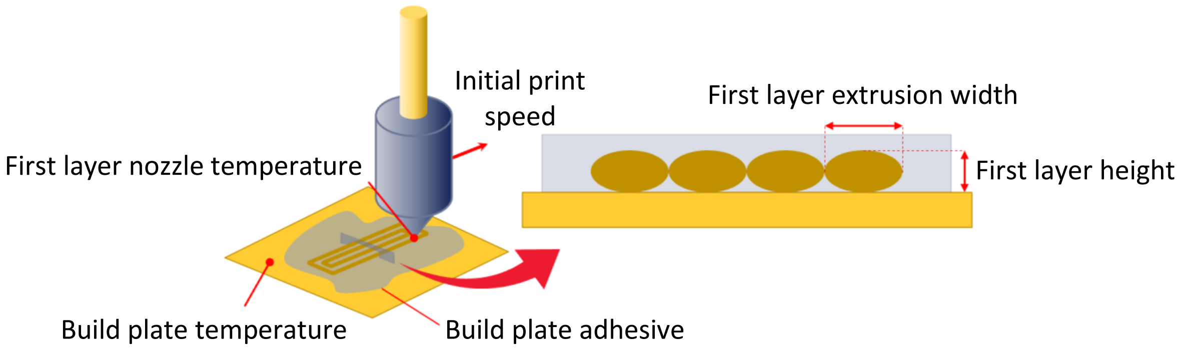

Figure 3.4. Schematic of the FFF process highlighting 6 key adhesion parameters.

Bed temperature is set to promote initial layer adhesion to the build plate. Keeping the layer at an elevated temperature minimises its thermal contraction which could otherwise cause mechanical debonding from the build plate. Adhesion can be further enhanced by coating the build plate with an adhesive prior to printing. Several parameters can be used to minimise cooldown, again for better bonding. Initial bead width and height can be increased for better heat retention and rigidity. Print speed can be lowered to decrease the viscoelastic stress applied to the solidified bead. This is especially important in curved raster paths where the print head can exert a sideways force on the bead printed a few moments prior. Finally, the initial layer temperature can be increased to help the bead spread by lowering its viscosity as it contacts the build plate.

3.2.2 Extrusion parameters

Extrusion settings largely depend on material selection. 4 key parameters are illustrated in Figure 3.5. The nozzle temperature must be set above the filament's melting point to ensure consistent extrusion with minimal back pressure. Excessive pressure in the hot end resulting from incomplete melting or high melt viscosity can cause slippage of the extruder gears, leading to under-extrusion. Nozzle temperature is typically provided by filament suppliers to be used as a starting point for experimental fine-tuning.

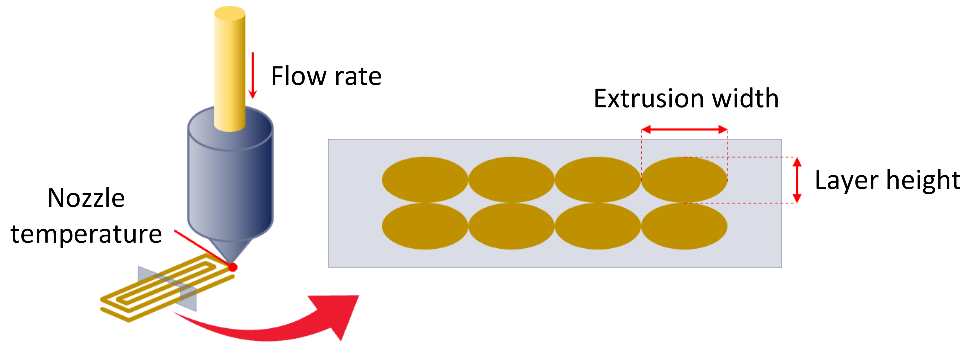

Figure 3.5. Schematic of the FFF process highlighting 4 key extrusion parameters.

Once the optimal nozzle temperature has been determined, the flow rate (or extrusion multiplier) can be determined and set. The flow rate is a percentage representing the number of motor steps needed to extrude a given length of filament. The default flow rate is 100%. A higher valuer (e.g., 105%) can be set to compensate for under-extrusion and vice-versa for over-extrusion.

When printing the bulk of the part, extrusion width is typically set as equal to the nozzle diameter or slightly higher to accommodate induced die swelling. Increasing the extrusion width will decrease the total number of beads in a single layer. It can be tuned to perfectly fill gaps in thin walls and match the geometry defined in CAD.

Layer height defines the increment by which the nozzle-bed distance is increased before printing a new layer. It does not affect how much the bead is "squished" (this is affected by the flow rate). It does however affect the amount of shear stressed developed inside the deposited bead which may affect inter-layer bonding characteristics. Layer height has a direct effect on print time and resolution. For example, bringing it down from 0.2 mm to 0.1 mm will double the Z-axis resolution of the part, but also double the print time since there will be twice as many layers to print.

3.2.3 Motion parameters

Motion parameters govern how the print head translates in its three degrees of freedom (Figure 3.6). These are typically tuned later in the process to decrease print time without compromising quality. Print speed is the horizontal travel speed of the head while it extrudes filament. While a higher print speed is desirable to minimise print time (and therefore cost), it increases the amount of viscoelastic stress applied to the part which increases the risk of defects. For this reason, low speeds are typically used for preliminary material tuning and progressively increased thereafter.

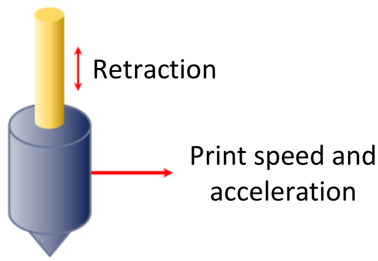

Figure 3.6. Schematic indicating 2 key motion parameters.

Pressure built up in the nozzle can cause material to ooze out during travel moves. This excess material can solidify and accumulate in an effect known as stringing. Although minimal stringing is easily sanded away, heavy stringing can cause significant surface defects and even print failure. This effect is mitigated using the slicer's retraction settings. With retraction enabled, the extruder will retract filament back to relieve nozzle pressure before travel moves and avoid oozing. Retraction distance and speed can be tuned to retract just the right amount of material. Properly tuned retraction settings can greatly improve surface quality and reduce post-processing time. This is demonstrated in Figure 3.7 where two samples were printed in carbon fibre-reinforced polyethylene terephthalate filament (PET-CF) on a BigRep Studio G2 printer. The first sample was printed using default settings with no retraction, resulting in heavy stringing. The second sample was printed with a retraction distance of 5 mm, retraction speed of 50 mm/s and vertical lift of 0.6 mm. With these settings, heavy stringing was eliminated. Although this effect is not the focus of this work, it must nonetheless be managed maximise print quality and minimise post-processing time.

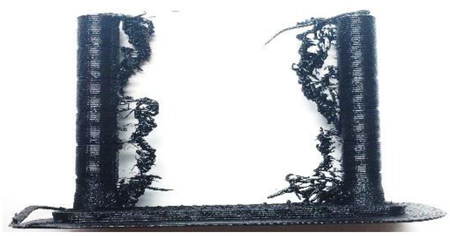

(a)

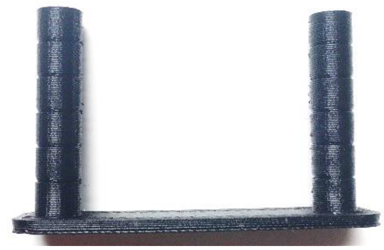

(b)

Figure 3.7. Before (a) and after (b) turning on retraction settings on a PET-CF print.

As seen in Section 2.1.5.2, motor acceleration is defined by a multitude of parameters, many of which are fixed and can only be edited by accessing the machine firmware. This is rarely possible in industrial FFF machines including open-source models. For example, the AON3D M2 only allows changes in maximum acceleration within an allowable range via the terminal window. To minimize print time, acceleration should be set as high as possible while taking care not to cause excessive vibration of the print head.

3.2.4 Feature parameters

A critical benefit of using a slicer for generating G code for FFF is the ability to create printed features without needing to model them in CAD. These features are generated algorithmically to make the process more efficient. Properly tuning these feature parameters result in significant cost and time saved as well as better print quality.

An important feature used in this work is support material. With supports enabled, the slicer will automatically detect geometries printed in mid-air (known as overhangs) and generate support structures below them. A key characteristic of effective supports is their ability to cleanly break off from the part, leaving minimal material residue and surface imperfections. To achieve this, the bond strength between the support and the overhang must be kept to a minimum. In other words, the support must get enough time to cool down before the first overhang layer is printed. This is done by defining separation layers in the slicer. When printing, the extruder will “skip” the specified number of layers before printing the overhang onto the supports. Effectively, separation layers increase both layer time and the vertical distance between printed beads to ensure a weak but still rigid bond is formed.

Another powerful slicer feature is the generation of infill. Solid CAD bodies can be printed hollow with sparse internal walls for structural integrity. This can dramatically reduce print time with little effect of print quality. infill density can be increased to meet mechanical performance requirements. However, parts printed in this work are mostly thin-walled bodies, making infill tuning less critical. The use of infill and supports is illustrated in Figure 3.8.

(a) (b)

Figure 3.8. Solid CAD model (a) and slice (b) of a shape requiring support material and infill.

3.2.5 Environmental parameters

Environmental conditions can have a strong impact on the performance and quality of printed parts. Ambient temperature and humidity must be carefully controlled to ensure print repeatability.

Chamber temperature provides a lower limit for the printed part to cool down to. An elevated chamber temperature allows high-temperature materials such as PEI to be printed with minimal thermal deformation. However, having it too high can cause the part to instead deform under its own weight. For this reason, low temperature materials such as PLA may require enhanced cooling using fans.

3.2.6 Custom parameters

Slicers offer varying degrees of toolpath customization in different stages of the printing process such as start, layer change, retraction, tool change and end. User-defined G-code scripts can be developed and inserted by the slicer to improve user experience, avoid collisions, and mitigate defect generation. This slicer feature is utilized in Section 5.2.

3.3 Key Performance Indicators

While process parameters are the inputs of the tuning process, key performance indicators (KPI) are the outputs. KPI's show at a glance how industrial open-source FFF compares to its competitors (proprietary industrial FFF and alternative processes such as injection moulding). KPI's in the context of business strategy and operations management are a broad topic beyond the scope of this work. The indicators listed in Table 3.1 are used to track the effects of modified process conditions. Each has an associated target defined in collaboration with the industrial partner as criteria for a viable process.

Table 3.1. KPI Targets

Property	Target	Ref.
Tensile modulus (Z)	2.392 GPa	[19]
Tensile strength (Z)	58.95 MPa	[19]
Thickness tolerance	3.2±0.4 mm	[5]
Width tolerance	13.0±0.5 mm	[5]

3.3.1 Mechanical properties

The mechanical properties in the Z-direction (or inter-layer properties) were chosen as KPI since they present the highest knockdown relative to neat injection moulding [19, 84]. Specifically, tensile modulus and tensile strength were selected. The associated test standard is ASTM D638 where a dogbone coupon is loaded in tension. Direct coupon printing was selected as manufacturing method. Although cutting them from a printed plate may be more representative of an end-use part, results from directly printed coupons are more readily comparable to literature values such a those of NCAMP.

Although usually associated with intrinsic material properties, tensile modulus has been shown to be affected by the process as well. A target modulus of 2.392 GPa was selected based on NCAMP's material qualification data report [19].

Interlayer tensile strength (or weld strength) is highly dependant on process parameters such as layer height and nozzle temperature which affect the degree of bead coalescence [85]. A target strength of 58.95 MPa was selected based on the same data report [19].

3.3.2 Dimensional tolerance

The printer's ability to print with tight dimensional tolerances is essential to make parts that assemble with other hardware such as bolts and electronic components. It is also an indication of good process repeatability. In this work, targets for dimensional tolerance were selected based on the width and thickness requirements for a standard dogbone coupon (see Figure 4.3). This way, dimensional KPI could be measured using the same tests as for mechanical properties.

3.4 Implicit Parameters

Determining the effect of each process parameter on KPI requires a rigorous DoE. A DoE requires several runs, the amount of which depending on the number of parameters and the DoE method chosen. For example, a Taguchi DoE with 11 two-level factors requires 12 runs. Since there is a benefit to minimize the required number of runs to reduce total experiment time and cost, parameters must be selected carefully to capture as much of the design space as possible.

Some parameters are neither clear inputs nor outputs but are nonetheless critical in understanding fundamental challenges of AM. In this work, the term "implicit parameter" refers to a process parameter that is not explicitly defined in the slicer settings but is a direct function of one or multiple of them. Varying implicit parameters in a DoE may require fewer runs and provide a more physics-based understanding of KPI. The following sections introduce two implicit parameters hypothesized to provide such an understanding.

3.4.1 Layer time

Layer time is simply the time required to print a layer of material. It mainly depends on layer size, toolpath, print speed, and acceleration. Layer time control is critical in large-scale AM where cooldown management plays a significant role in process optimization. To recall from Section 2.1.3, Compton et al. [34] specifically varied layer time to find the optimal setting long enough to avoid warping and short enough to avoid cracking. In metal wire feed AM, layer time is a critical parameter due to its impact on interpass temperature (the temperature of the material right before being printed on) [86]. There appears to be less emphasis on layer time in conventional scale FFF research.

Layer time control in FFF slicers is limited. The Cura slicer enables the user to define a minimum layer time to control cooling. If a layer is calculated to require less time to print with current settings, the print speed will decrease to meet the minimum layer time requirement. To avoid excessive under-speed, a minimum speed is also defined. If it is reached, the print head will lift away from the part to meet the minimum layer time. This algorithm is illustrated in Figure 3.9 using a triangular part as an example. The same caped under-speed is available in Simplify3D, but not the head lift feature.

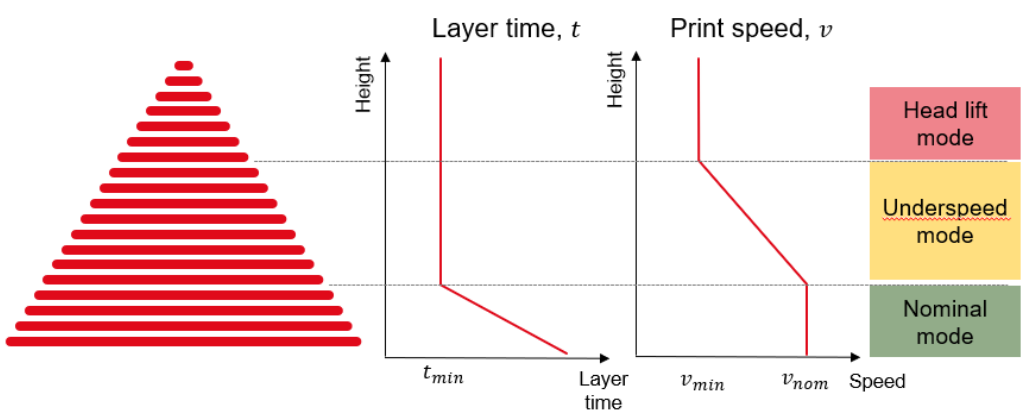

Figure 3.9. Layer time control algorithm as implemented in Cura.

Tuning this feature can prevent heat build-up in small layers which would otherwise result in warping. This was demonstrated by printing two conic samples in PET-CF on a BigRep Studo G2 printer. The first sample (Figure 3.10a) was printed at a constant speed of 77.5 mm/s as per default settings. The top 30% of the sample showed significant warping and layer fusion. The second sample (Figure 3.10b) was printed while imposing a minimum layer time of 3 s and minimum print speed of 20 mm/s with head lift enabled. The quality of this sample was noticeably higher than the first, with consistent layer lines throughout its height. This is a demonstration of the impact of layer time on visual quality. This work will aim to also evaluate its effect on mechanical properties.

(a) (b)

Figure 3.10. Conic sample printed in PET-CF without layer time control (a) and with a minimum layer time of 3 s, minimum speed of 20 mm/s and head lift enabled (b).

3.4.2 Thermal gradient

Any variation in temperature with respect to space is known as a thermal gradient. Thermal gradients are also a driving force of heat transfer. In FFF, the traveling toolhead creates a significant thermal gradient between the polymer melt being deposited and the layers beneath it. As a result, this temperature variation dictates the rate at which the extruded material solidifies into a rigid bead. Toolpath and geometry cause the thermal gradient to also vary in time. In larger geometries, longer layer times allow increased cooldown between passes. As a result, wider variations in thermal gradient can occur. Because of its influence on the rate of solidification, the thermal gradient created from successive layer deposition and solidification is hypothesized to impact the degree of coalescence and bonding between layers. This would imply a significant correlation between measured thermal gradient and inter-layer mechanical properties.

Like layer time, thermal gradient is not explicitly controlled in the printing process. Instead, it varies as a function of the slicer settings and environmental conditions. Given the mathematical formulation of the diffusion of heat, where T is temperature, t is time, α is the thermal diffusivity constant, and x, y and z are spatial variables,

$$\frac{1}{\alpha}\frac{\partial T}{\partial t} = \frac{\partial^2 T}{\partial x^2} + \frac{\partial^2 T}{\partial y^2} + \frac{\partial^2 T}{\partial z^2} \quad [1]$$

it is natural to expect said diffusion to depend on parameters related to time, space and temperature. The specific parameters expected to affect the thermal gradient during layer deposition include layer time, print speed, layer height, extrusion width, as well as temperatures of the nozzle, chamber, and bed. It is hypothesised that layer time will have a significant effect on interlayer thermal gradient as it captures the effect of geometry and print speed. If this relationship could be demonstrated, continuous monitoring of layer time and thermal gradient could be proposed to provide relevant data to certify the mechanical properties of printed parts without resorting to destructive mechanical testing.

4 PROCESS EVALUATION

This chapter documents the experimental evaluation of the FFF process carried out on an AON3D M2 printer using ULTEM 9085 PEI filament. Although the suppliers of both products recommend processing conditions for optimal quality, post-purchase tuning was still required to ensure process repeatability and gather data on the effect of different conditions. The goal of this evaluation was to gain a further understanding of the printer behaviour and defects to correct. A combination of test coupons and end-use parts were printed to test a range of features and parameters. The objective of this chapter is ultimately to determine the parameters and features requiring additional tuning so that they do not impede the formal characterization process.

4.1 BENCHMARK TEST FOR PRINT QUALITY

Benchmark print geometries are common in consumer grade FFF [87] and AM research [88-90]. They allow users to quickly evaluate the capability of 3D printing systems to accurately reproduce features given the hardware and print settings. The 3D Benchy is a publicly available benchmark print geometry commonly found in online forums and tutorials [91]. Its features help evaluate the capabilities of machines, materials, and processes. It was selected as preliminary print geometry to evaluate the default print settings provided by the printer manufacturer.

A model of the default 3D Benchy is illustrated in Figure 4.1. The following features were of interest to evaluate the print quality of default parameters:

- Hull: its smooth overhanging upcurve will reveal surface deviations which can be caused by improper temperature or extrusion settings, or overly compliant hardware.
- Side-facing holes: their embossed contours show whether the printer can resolve features as small as 0.30 mm.
- Chimney: its 7.00 mm outer diameter can result in low layer times which can result in heat accumulation and warping if layer time settings are not well tuned.

(a) (b)

Figure 4.1. Side view (a) and isometric view (b) of 3D Benchy model highlighting key features which help evaluate print quality.

The model was sliced and printed using the settings in Table 4.1. A side view of the result is shown in Figure 4.2. The hull layers were consistent with minor imperfections in extrusion start and stop areas. Side-facing holes showed light stringing which was readily sanded off. Overhangs drooped slightly but did not cause defects in subsequent layers. The chimney had notable warping and excessive layer fusion. Overall, this print demonstrated the capability of the default settings to print cleanly without the need for systematic retraction and overhang tuning. Most notable defects were observed in areas of low layer time, indicating the need to better understand the cooling process taking place in high-temperature FFF.

Table 4.1. Main Process Parameters for Printing the 3D Benchy Model

Parameter	Value
Drying cycle	16h at 70°C
Build plate adhesive	Yes
Nozzle temperature	350°C
Bed temperature	180°C
Chamber temperature	120°C
Layer height	0.2 mm
Extrusion width	0.4 mm
Nozzle diameter	0.4 mm
Print speed	30 mm/s
Infill density	35%
Infill pattern	Rectilinear

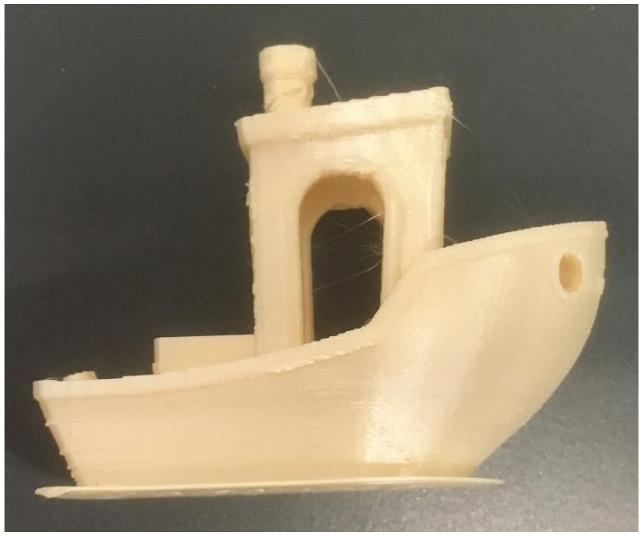

Figure 4.2. Printed 3D Benchy model.

4.2 Vertical Tensile Coupon

The next part to be tested was the ASTM D638 tensile coupon printed perpendicular to the build plate. As this geometry was selected for mechanical testing, preliminary testing was first carried out to ensure the part met dimensional tolerances and no defects would cause premature failure. The vertical tensile coupon is a tall slender part with strict dimensional tolerances. Slender parts can bend under the lateral loads exerted by the extruder which can be source of defect or even print failure. In the case of the ASTM D638 sample, the overall length must be at least 165 mm while the thickness must be 3.2±0.4 mm and the gauge width 13.0±0.5 mm (complete dimensions are provided in Figure 4.3). The part was printed in commercially available ULTEM 9085 PEI. The filament was first dried overnight at 70°C. Print parameters provided by AON3D were used as starting point for preliminary testing as for the 3D Benchy. Main settings are listed in Table 4.2. The only parameter that was modified was the infill. A 100% dense concentric infill was used instead of a rectilinear infill (Figure 4.4) to minimise vibrations caused by frequent cornering of the tool head. This was programed in Simplify3D by increasing the number of outline shells to 5, resulting in a fully dense part regardless of infill settings.

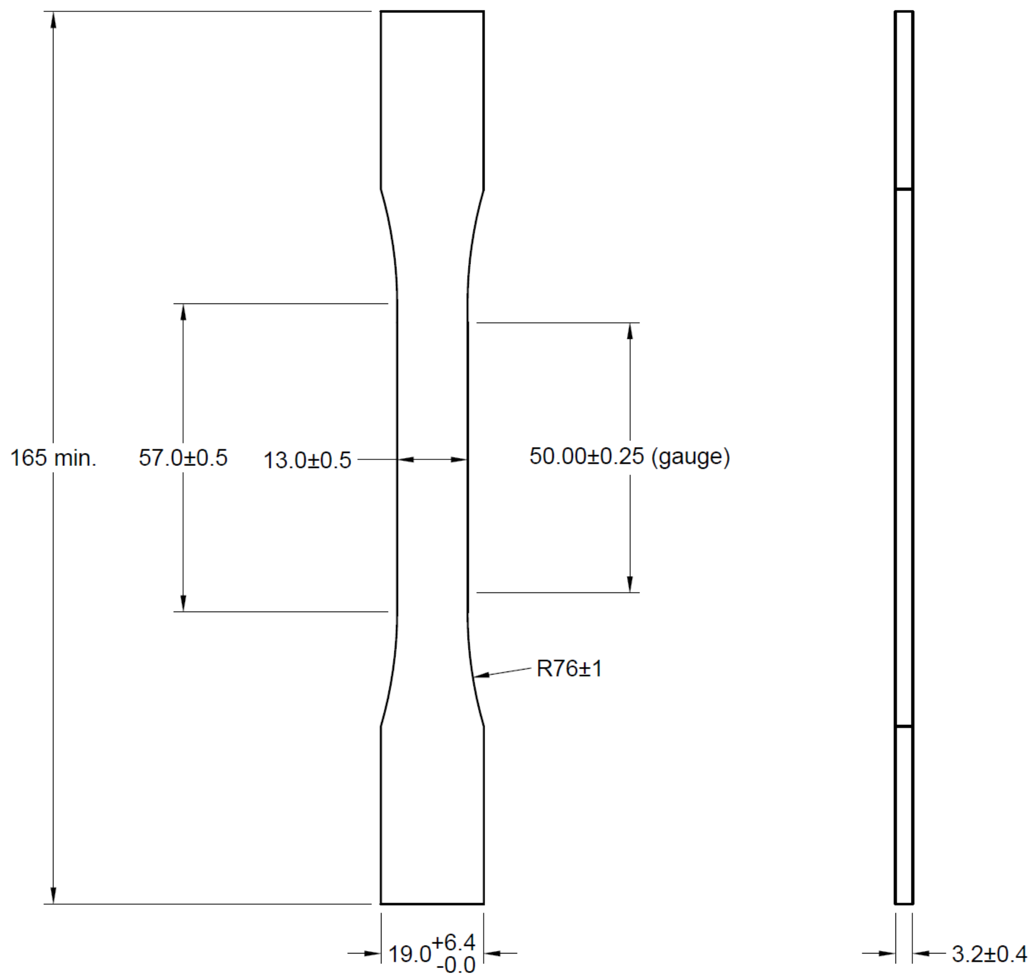

Figure 4.3. Vertical tensile coupon dimensions [5].

Table 4.2. Main Process Parameters for Preliminary Printing of the Vertical Tensile Coupon

Parameter	**Value**
Drying cycle	16h at 70°C
Build plate adhesive	Yes
Nozzle temperature	350°C
Bed temperature	180°C
Chamber temperature	120°C
Layer height	0.2 mm
Extrusion width	0.4 mm
Nozzle diameter	0.4 mm
Print speed	30 mm/s
Infill density	100%
Infill pattern	Concentric

(a) (b)

Figure 4.4. Concentric (a) vs rectilinear (b) dense infill patterns for a single layer of an ASTM D638 vertical tensile coupon.

These print settings resulted in a successful print with notable defects. The tall slender geometry was stable initially but oscillated under nozzle motion in the final 20% of printing. This caused layer imperfections which could impact strength and grip hold. To stabilize the structure during printing, side supports were added on either side of the coupon. Side supports were printed using the same material and overall settings as the part itself. A horizontal offset of 0.20 mm from the main part ensured they could be broken off cleanly. Side supports were programmed in Simplify3D by placing a 25 mm x 3 mm rectangular model above the coupon and generating supports automatically (Figure 4.5). To minimise material waste and post-processing time, the machine was programmed to stop printing at a height of 165 mm once the coupon was fully printed. The result of this modification can be seen in Figure 4.6 and Figure 4.7.

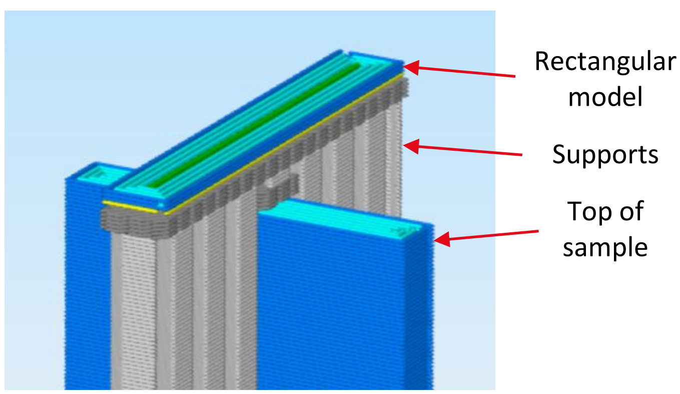

Figure 4.5. Supports generated by the rectangular model acted as coupon side supports.

To maximise print quality while minimising print time, support raster angles of -45° and 90° were tested. The 90° raster printed 10% faster but resulted in heavy stringing in the upper section of the coupon (Figure 4.6). As a result, the coupon printed with the default angle of -45° was selected for further testing (Figure 4.7).

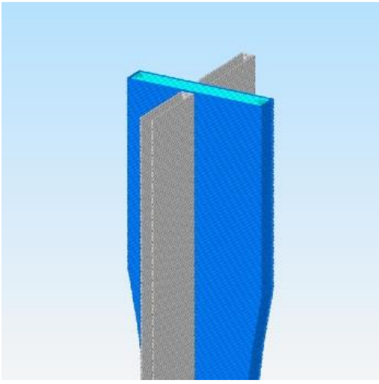

(a)

(b)

Figure 4.6. Slice (a) and test print (b) of side supports with 90° raster angle.

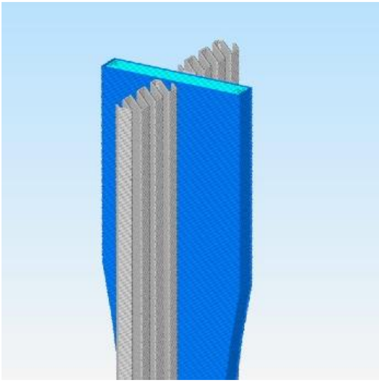

(a)

(b)

Figure 4.7. Slice (a) and test print (b) of side supports with -45° raster angle.

4.3 Process Assessment

Preliminary printing of the 3D Benchy model and vertical tensile coupons provided insights into what aspects of the FFF process were reliable enough for formal characterization and those requiring improvement. The default process temperatures, print speed, extrusion width, and layer height resulted in uniform visual surface quality free of major defects such as burns or warping. However, key issues were identified as problematic. In the following chapter, these will be addressed and resolved:

- The print head lacked rigidity, causing it to vibrate during rapid direction change and slip on some occasions where nozzle pressure built up prior to printing. These problems were partly attributed to the loosening of the single set screw holding the cooling block in place.
- The AON3D M2 machine has spools mounted on the back panel, exposed to ambient humidity which dried PEI filaments readily uptake over the duration of the print.
- The default starting toolpath generated by Simplify3D commanded the print head to enter the print area with no vertical offset, causing it to collide with the bed on multiple occasions.
- The bed temperature and adhesive used provided reliable layer adhesion. The default profile was deemed acceptable for tall slender geometries such as the vertical tensile coupon.

5 PROCESS TUNING

In this chapter, issues noted during the process evaluation phase are addressed. Having a robust process to create defect-free parts as quickly and efficiently as possible will reduce down-time and trial-and-error during the characterization phase. Improvements are implemented in the areas of hardware, toolpath, and process parameters. Methods for thermal gradient monitoring and coupon characterization are also tested.

5.1 HARDWARE IMPROVEMENTS

Although built for industrial capability, the M2 could benefit from key design changes to improve its robustness and effectiveness. The two following changes were chosen due to their ease of implementation and high improvement potential.

5.1.1 Print Head

The first hardware improvement targeted print head rigidity. To print at high speed with minimal vibration, compliance of the print heat must be minimal. Out of the box, the inline cooling block is connected to the probe collar via a single set screw which was found to loosen as a result of temperature cycling and rapid changes in direction. On multiple occasions, this caused the hot end to shift out of alignment when material was extruded. Compliance of this joint was significantly reduced by adding a second set screw to the assembly using a conventional milling machine (Figure 5.1).

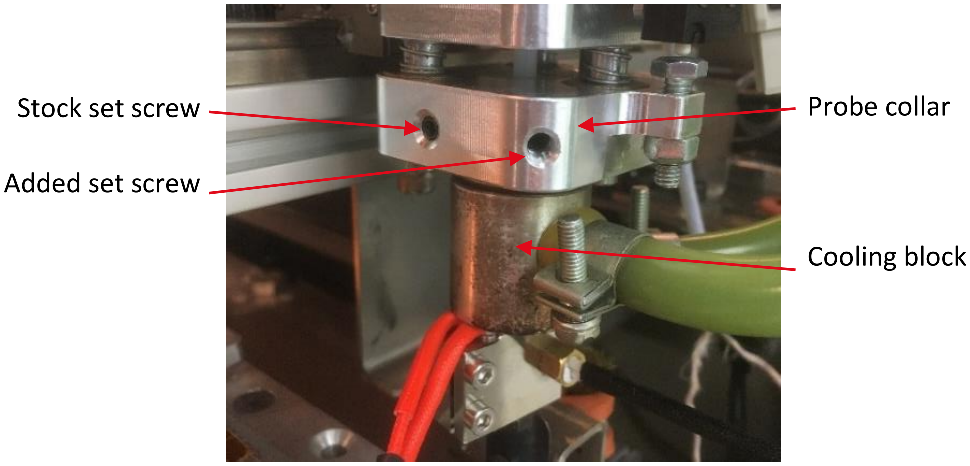

Figure 5.1. Print head assembly with second set screw holding the cooling block to the extruder assembly.

5.1.2 Spool Storage

By default, the filament spool holders on the AON3D M2 are mounted at the back of the machine. To avoid exposing spools to atmospheric humidity, a metal spool holder was placed inside the machine (Figure 5.2). Although this solution reduced the maximum build height by 40%, this was not an issue considering most parts expected to be printed on this machine did not require a full envelope. In addition to keeping the filament dry during printing, this allowed the printer to be used as an oven to dry filaments prior to printing. This also added the safety benefit of not having to handle hot filament from an oven to the printer.

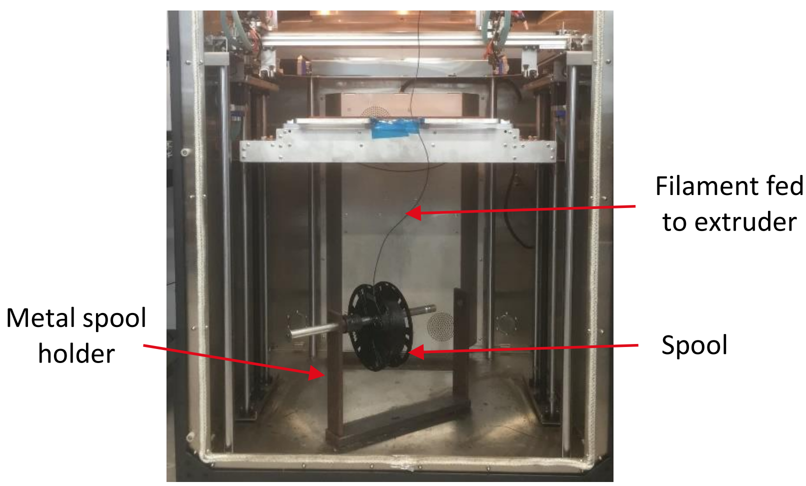

Figure 5.2. Internal metal spool holder added to actively dry filament during printing.

5.2 Toolpath Improvements

Key issues recorded during the process evaluation phase required modification of the G code fed to the printer. This was achieved by writing scripts and adding them to the profile's custom settings.

5.2.1 Starting Script

An issue encountered repeatedly during testing was the collision of the nozzle with the edge of the build plate. The printer's probing feature measures the bed position where the print will take place, but not along the edge (Figure 5.3). As a result, minor undulation in the surface could cause the nozzle to scrape higher areas at the start of printing which could shift the hot end out of alignment. To mitigate this, the following G code script was written.

```
G1 Z5.0 F1000; Drop bed by 5mm at 1000mm/s
G1 X225.0 Y100 F3000; Go to bed centreline at 3000mm/s
```

These lines were executed just before the first printing command. When the print head was ordered to approach the bed and begin extrusion, it was sure to be in a probed area where bed position was known. This made the nozzle stay away from the bed in areas not previously probed and avoid collisions.

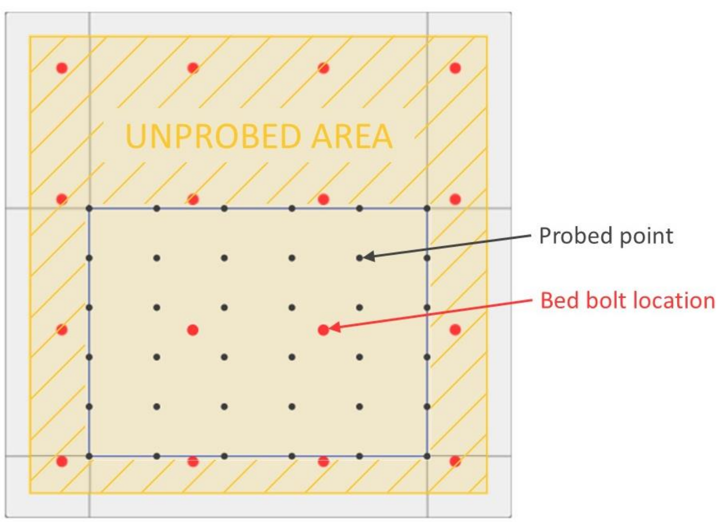

Figure 5.3. Screenshot of the AON3D user interface with emphasis added to probed and unprobed areas.

5.2.2 Ending Script

With prints often having to print overnight, it was common to have the printer completely cooled down to room temperature when retrieving the part. This posed two issues: (1) the filament had solidified inside the hot-end and could not be removed without re-heating it, and (2) the cold enclosure could allow moisture to contaminate the filament. To solve these issues, a two-part ending script was added to the profile's custom settings. First, the filament was retracted from the hot end area to prevent it from bonding to it when solidifying.

```
G91; set to relative positioning mode
G1 E-30 F180; retract 30mm
G90; set back to absolute positioning mode
```

Second, all temperature controllers were shut down except for the chamber which was maintained at 70°C to actively dry the filament upon print completion.

```
M104 T0 S0; turn off T0 heater
M104 T1 S0; turn off T1 heater
M104 T2 S70; set chamber temperature controller to 70C
M140 S0; turn off bed heater
```

This script allowed for significant time savings over the course of the following experiments by speeding up the filament swap process and eliminating the need to re-dry the filament before printing another part.

5.3 Initial Layer Calibration

To achieve the best possible initial layer quality and adhesion, optimal parameters were determined using a DoE. The parameters studied were initial raster height and width, nozzle temperature, and bed temperature. Other parameters were held constant at their default values (see Table 4.2). The material used was ULTEM 9085 PEI. Parameter levels are listed in Table 5.1. The difference between levels was maximized to so their effect could be isolated from random process variability. The minimum bed temperature was set as the default value and average T_g measured by Tao [81]. Its maximum was set as the machine's highest possible temperature to promote layer healing. The minimum raster width was set to 112.5% of the nozzle diameter to accommodate dye swelling. It was increased to 137.5% to maximize contact area with the bed. Nozzle temperatures were selected based on minimum and maximum values in the range of default settings. Layer height was maintained below raster width to ensure bead was sufficiently squished by the nozzle to promote adhesion. I was set to 44.4% of raster width in level 1 and 63.6% in level 2.

Table 5.1. Initial Layer Parameter Levels

Parameter	Level 1	Level 2
Bed temperature (°C)	180	200
Raster width (mm)	0.45	0.55
Nozzle temperature (°C)	350	390
Layer height (mm)	0.20	0.35

5.3.1 Trials

Runs were defined based on the corresponding orthogonal array following the Taguchi method. For each run, four single layer 75 x 10 mm rectangular coupons were printed. A chamber temperature of 120°C and print speed of 30 mm/s were held constant. Bed adhesive was applied before each run. The printer was pre-heated for 1h before starting the experiment. Runs were performed in order with 10 min. breaks in between to allow the temperature to stabilise. Between runs 4 and 5, the bed was left to heat up for 30 min. Coupons were removed using a metal scraper and stored for analysis.

Table 5.2. Initial Layer Trials

Run	Bed Temp. (°C)	Raster width (mm)	Nozzle Temp. (°C)	Layer height (mm)
1	180	0.45	350	0.20
2	180	0.45	350	0.35
3	180	0.55	390	0.20
4	180	0.55	390	0.35
5	200	0.45	390	0.20
6	200	0.45	390	0.35
7	200	0.55	350	0.20
8	200	0.55	350	0.35

Visual inspection of the coupons was done first with the naked eye and second using a Nikon Eclipse L150 optical microscope with a Nikon LU Plan Fluor 5x magnification lens. The coupons were placed one at a time on the stage without slides or casting. Individual photographs were captured to highlight key coupon features such as raster gaps. Using the DCI Capture software, the ruler tool was used to manually measure raster gaps in each image as shown in Figure 5.4. Coupon thickness was measured in the 3 locations shown in Figure 5.5 using a digital micrometer.

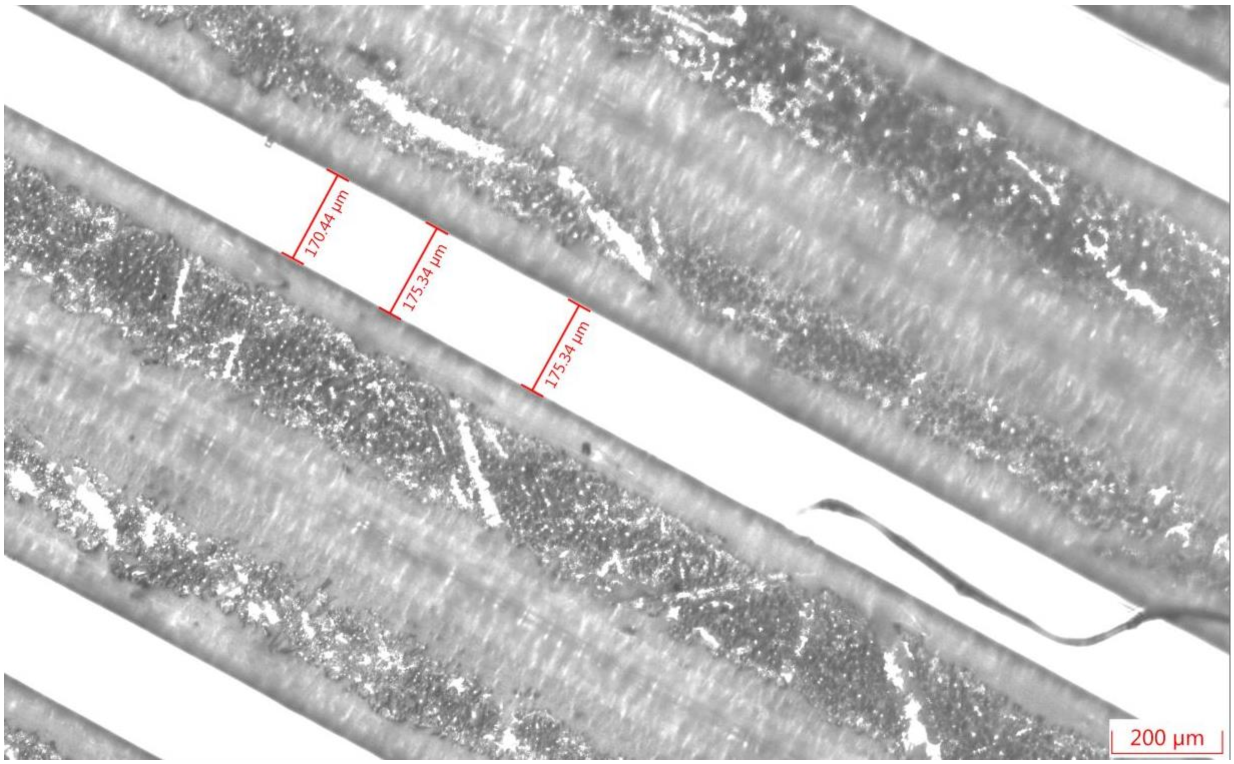

Figure 5.4. Sample optical micrograph from run 7 illustrating the raster gap measurement method.

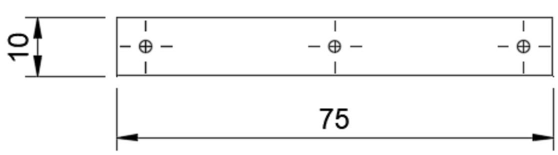

Figure 5.5. Initial layer coupon drawing showing position of 3 thickness measurements as hole marks (left, middle and right).

5.3.2 Results and Discussion

All runs cleanly separated from the bed except for run 5 which required significant scraping, resulting in raster separation (Figure 5.6). Each coupon received a general layer quality score out of 10. Points were allotted based on layer smoothness, absence of raster gaps, geometric consistency, and structural integrity. Overall scores and measurements are listed in Table 5.3. Sample optical micrographs for each run are provided in Figure 5.7.

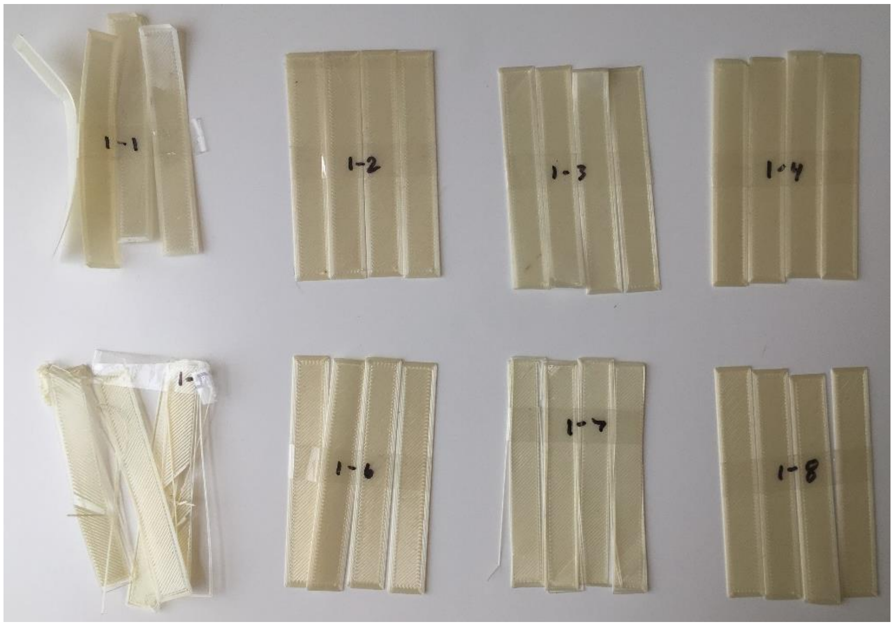

Figure 5.6. Initial layer coupons grouped and ordered by run from left to right, top to bottom.

Table 5.3. Initial Layer Results

Run	Max. raster gap (µm)	Avg. thickness delta (mm)	Quality score (/10)
1	100.57	0.035	6
2	0.00	0.080	9
3	176.73	0.064	5
4	0.00	0.106	9
5	>1000.00	0.126	1
6	109.40	0.142	4
7	241.20	0.125	2
8	133.63	0.129	6

(a) Sample optical micrograph of run 1.

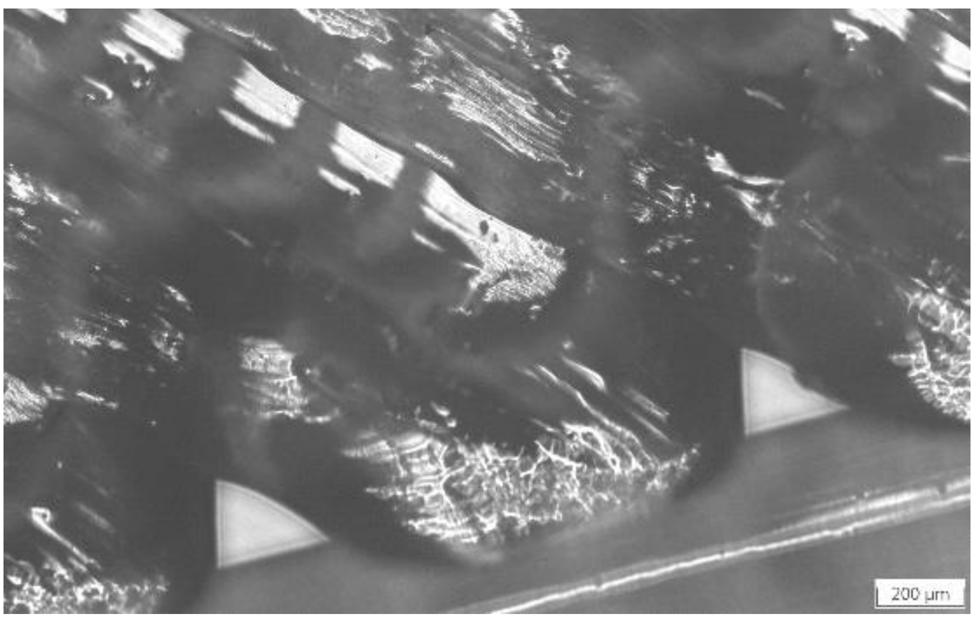

(b) Sample optical micrograph of run 2.

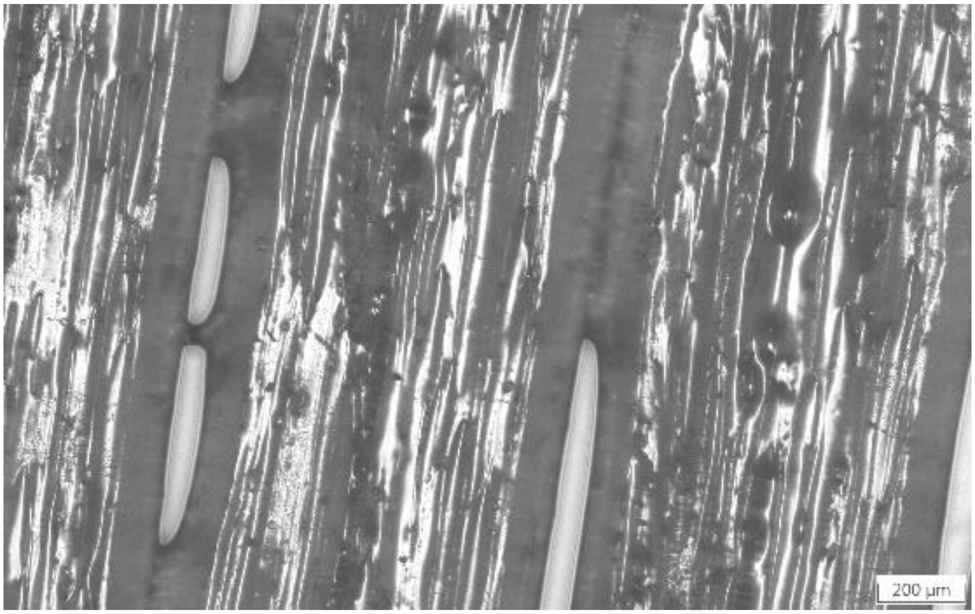

(c) Sample optical micrograph of run 3.

(d) Sample optical micrograph of run 4.

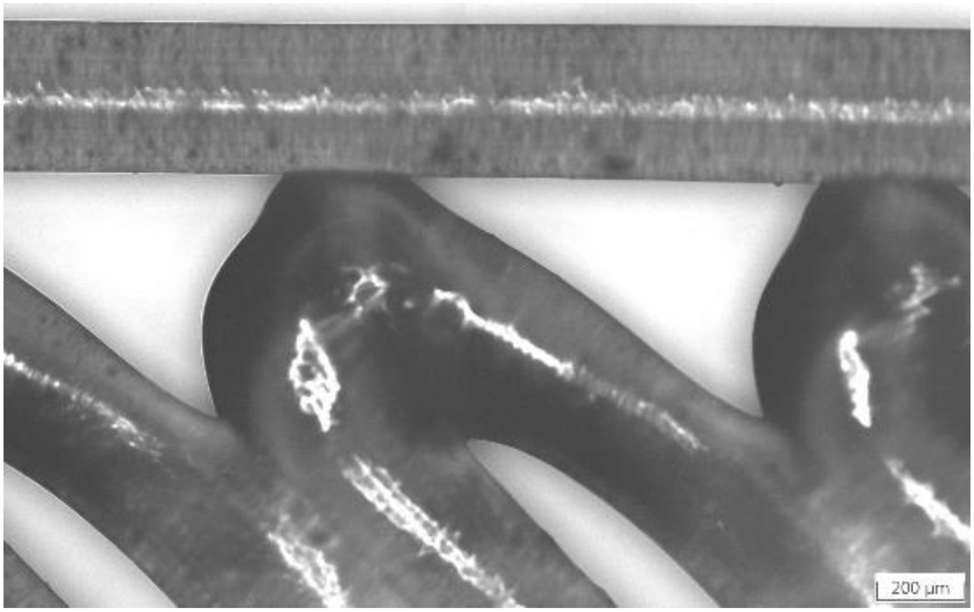

(e) Sample optical micrograph of run 5.

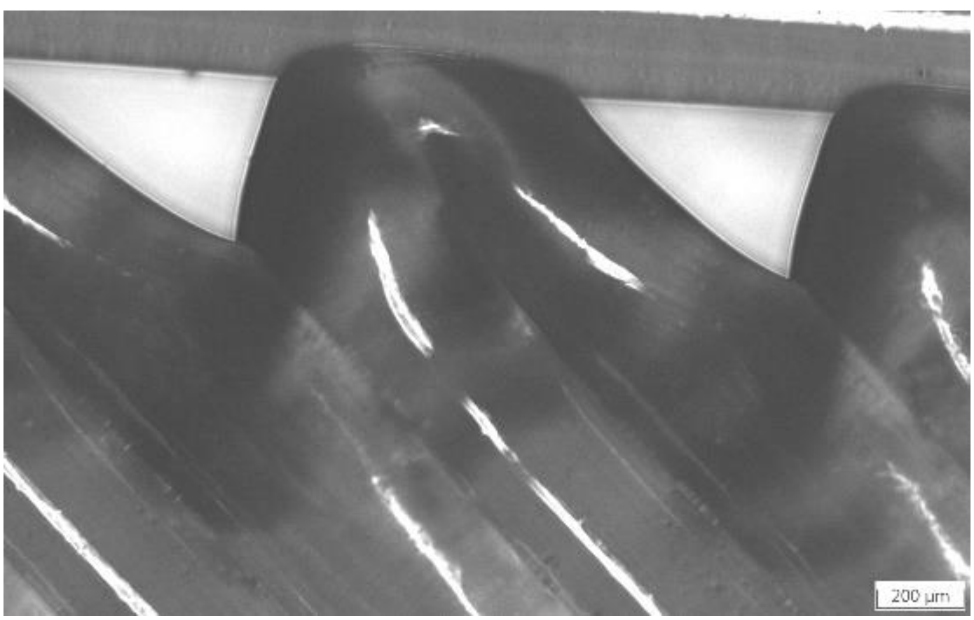

(f) Sample optical micrograph of run 6.

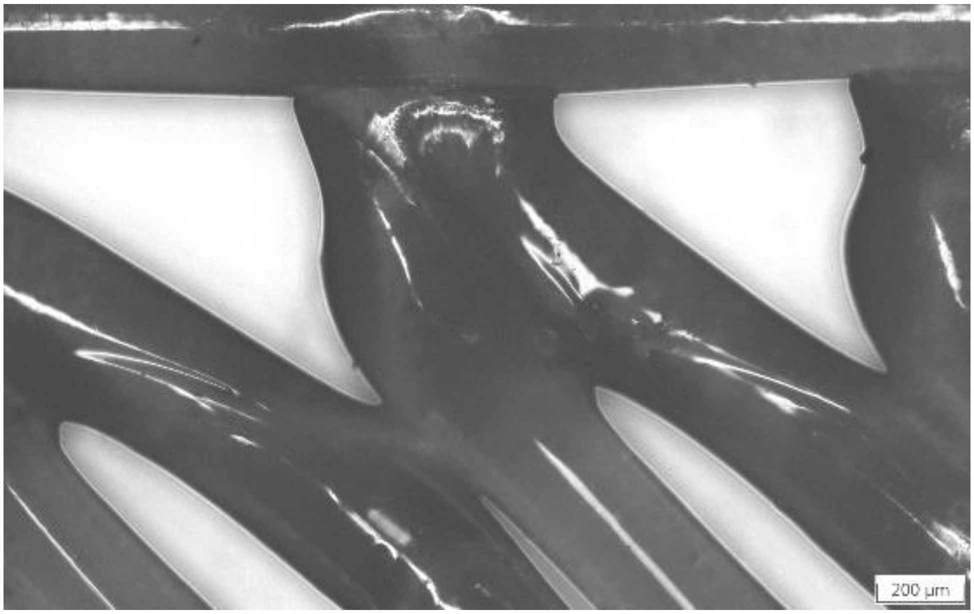

(g) Sample optical micrograph of run 7.

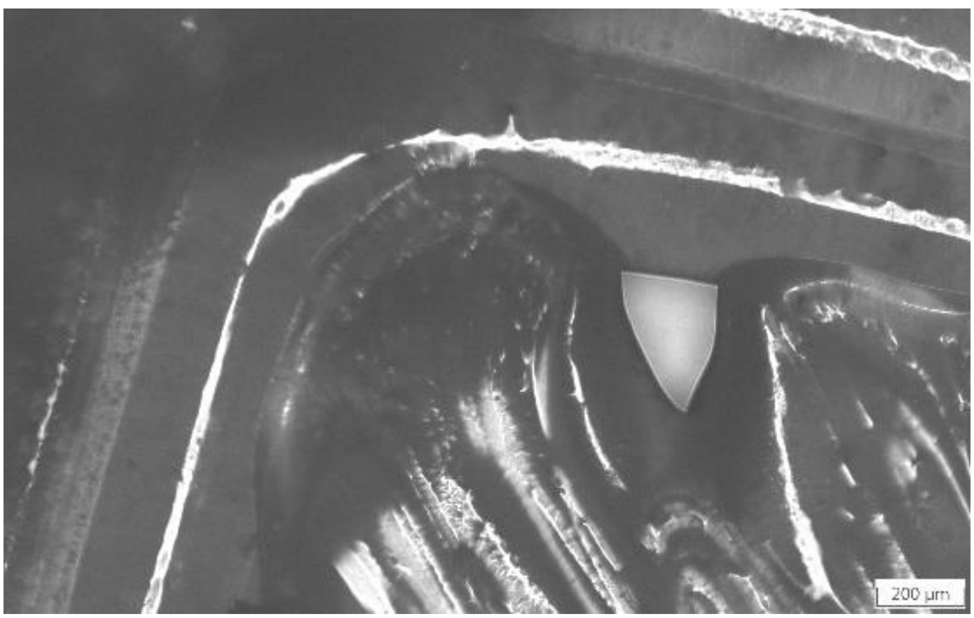

(h) Sample optical micrograph of run 8.

Figure 5.7. Sample optical micrographs of initial layer coupons.

Overall layer quality was better for thicker samples printed at lower bed temperature (runs 2 and 4 respectively shown in Figure 5.7b and Figure 5.7d). This observation was verified by one-way analysis of variance (ANOVA) using an alpha of 0.05. Runs which showed a significant difference between parameter levels ($P \leq \alpha$) were in fact bed temperature and layer height (Table 5.4).

Table 5.4. Initial Layer ANOVA Results

Parameter	P-Value
Bed temperature	0.038
Raster width	0.83
Nozzle temperature	0.66
Layer height	0.029

At elevated bed temperatures, inconsistent bonding was observed to occur between adjacent beads. In runs 5 to 8 (Figure 5.7, e to h), a gap consistently appears every 2 beads. This phenomenon is hypothesised to have occurred because of coalescence of the printed bead with the one next to it. This effect does not occur at lower bed temperatures because the melt cools down quicker and has a higher viscosity during deposition. In runs 5 to 8, the heat from the bed was enough to maintain a low viscosity, allowing beads to coalesce under capillary action before solidifying. Printed beads were thus shifted sideways and were too far away to connect with the next one, resulting in a gap every 2 beads. Although capillary forces contribute to inter-bead strength, it appears that letting them dominate the printing process results in significant dimensional inaccuracies.

5.3.3 Conclusion

Parameters having a significant effect on initial layer quality were bed temperature and layer height, with 180°C and 0.35 mm being respectively chosen for subsequent experiments. Significant capillary action was observed at higher bed temperatures, the effect of which would have to be studied in the context of a future project.

5.4 Development of Thermal Monitoring Method

The final process evaluation step was that of thermal gradient measurement. Since no such procedure is standardized in the literature, an in-house method was developed.

5.4.1 Low Temperature Method

Preliminary tests were done at low temperature using PLA instead of ULTEM 9085. This allowed the machine to print parts with the door open so the thermal camera could be placed directly in front of it at minimum focal distance to achieve maximum resolution (Figure 5.8a). Using this setup, a series of vertical tensile coupons were printed in PLA with default settings and no lateral supports.

(a)

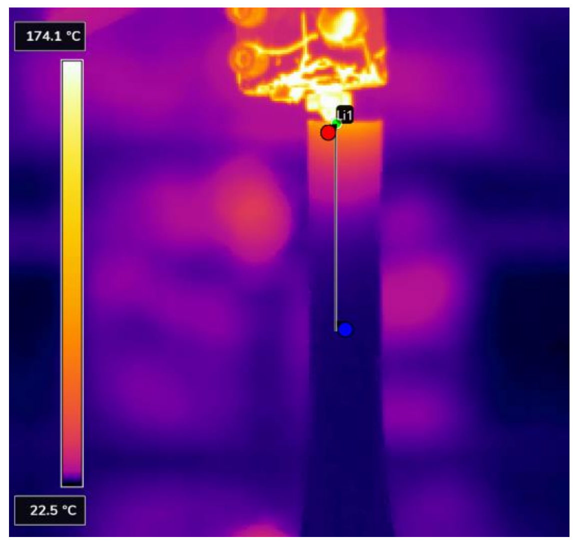

(b)

Figure 5.8. Low-temperature thermal monitoring apparatus (a) and sample thermogram of a PLA vertical tensile coupon (b).

Sample thermograms captured during printing were imported to FLIR Thermal Studio for analysis. The vertical thermal profile was extracted using the line tool (Figure 5.8b) and exported to CSV format. In Excel, the first 8 points were used to compute the thermal gradient by linear regression (Figure 5.9). Downstream position was converted from pixels to mm by measuring the width of the coupon in pixels using the line tool and in mm using a digital caliper.

From these preliminary results, it was concluded that this method was effective at measuring thermal gradients at low temperature and ready to be adapted to high temperature printing.

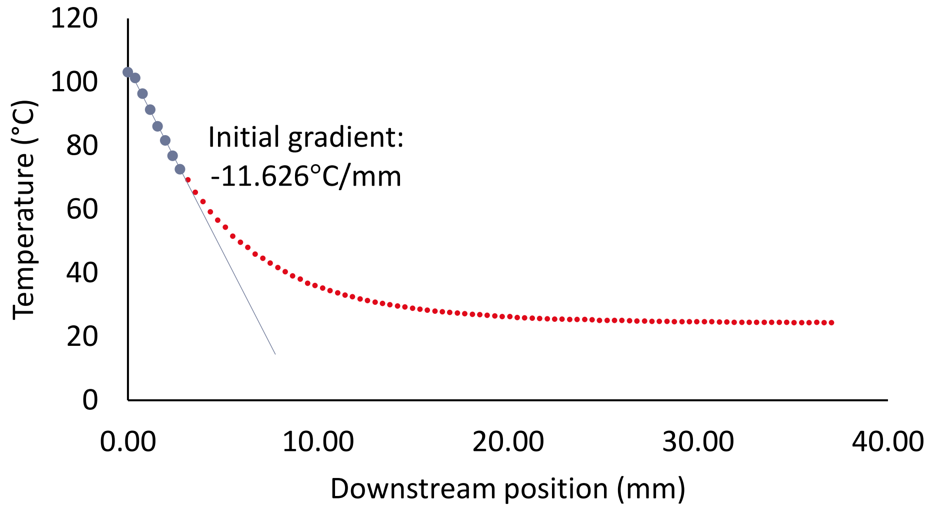

Figure 5.9. Sample thermal profile and thermal gradient result.

5.4.2 High-Temperature Method

There is a challenge in performing IR thermography while printing materials requiring a heated chamber. Since the FLIR T420 has a maximum operating temperature of 50°C, it cannot be placed inside the 120°C chamber when printing ULTEM 9085. Moreover, the double-pane glass and Lexan (PC) window of the AON3D M2 is IR opaque. As a result, thermal images cannot be captured through it. For these reasons, a high-temperature thermal gradient measurement method was developed and tested.

A vertical tensile coupon was sliced following the method of Section 4.2 with lateral supports printed at a raster angle of -45°. It was printed along the centerline of the build plate, 100mm from the front edge. The FLIR T420 camera was mounted on a tripod and adjusted to be level with the plane of the nozzle. The mounted camera was positioned near the door latch, 0.8m away from the print area. Thermograms were captured by opening the door by 0.2 m for 10 to 15 s to capture an image of the print and immediately closing it again. The chamber temperature was recorded before and after the operation. A thermogram was captured at 30%, 50%, and 70% of build completion.

With each measurement, a temperature drop of 10.5°C was recorded. Thermograms were imported into FLIR Thermal Studio for analysis. The box tool was used to select the pixels capturing the temperature of the coupon excluding supports (Figure 5.10a). The data contained in the selected region was then exported in CSV format to be processed using a Python script. Entries in each row were first averaged out to a single value. The resulting column vector was used to plot the average surface temperature as a function of distance away from the nozzle in pixels. The first 6 points were used to compute the thermal gradient by linear regression (Figure 5.10b).

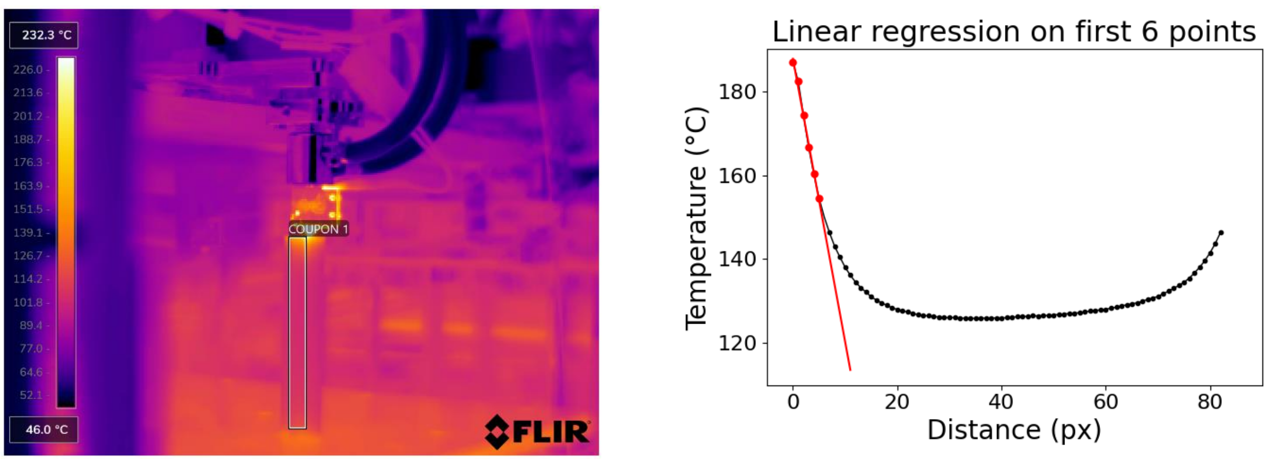

(a) (b)

Figure 5.10. Vertical thermal profile of ULTEM 9085 coupon showing a linear regression on the first 6 points.

Measuring the thermal gradient in high-temperature FFF is a challenge because the window is IR opaque. This problem was avoided by briefly opening the door for just enough time to capture a single thermogram. The drop in chamber temperature recorded with each run was deemed to have little impact on the temperature of the print itself. As a result, it was selected for thermal gradient characterization in the following chapter. However, this method is not suited for continuous thermal monitoring and can only provide readings at 5-minute intervals to avoid impacting the average temperature of the chamber.

6 Effect of Thermal Gradient on Weld Strength

This section describes in detail the steps taken to manufacture the test specimens, measure their processing conditions, and mechanically test them. It builds on the conclusions drawn from the process evaluation and tuning stages for maximum part quality and repeatability. In Chapter 3, weld strength was hypothesized to be a critical property of printed parts highly dependent on processing conditions. In this section, this dependency is studied experimentally through process monitoring and mechanical testing. A procedure is developed to print coupons at elevated temperature while measuring their temperature distribution using IR thermography. Thermal gradient is computed from temperature data using a Python script. The resulting vertical tensile properties are then measured and correlated with process data by analysis of variance.

6.1 Experimental Objective

The objective of this experiment is to determine the effect of the inter-layer thermal gradient during the deposition of fused filament on the resulting tensile strength and stiffness. Although the inter-layer tensile strength is one of many mechanical properties which would need to be certified for aerospace part qualification, it was selected for this study due to its expected dependency on processing conditions. Thermal gradient was selected as the parameter to be varied between runs. It is expected to capture the effect of different rates of heat transfer on the development of a strong bond between layers. The print parameters expected to impact thermal gradient are layer time, chamber and extrusion temperatures, print speed, and layer height and width. Layer time was chosen as the parameter to vary between runs due to its wide allowable processing window. Others were held constant to minimize the risk of print failure during trials.

6.2 Method

The experimental method was developed based on that used in Chapter 4 and improved upon in Chapter 5. Coupon geometry was held constant across trials to purely examine the effect of processing conditions. To vary the layer time without changing the print speed or geometry, coupons were printed simultaneously in batches of different sizes. Since printer grease was noticed to degrade with extensive high temperature printing, thorough preventative maintenance was carried out before running the experiment.

6.2.1 Material Selection and Conditioning

The material used was ULTEM 9085 PEI filament. Upon reception, the spool was removed from its packaging and dried in a convection oven for 16h at 70°C. It was then immediately loaded into the printer which was maintained at a minimum of 70°C throughout the duration of the experiment.

6.2.2 Trials

Experimental runs consisted in printing vertical tensile coupons under identical processing conditions, varying only the number of coupons printed at once. Using Fusion360, the coupon geometry was modeled based on the nominal dimensions of an ASTM D638 Type I coupon. The model was imported into Simplify3D in STL format and sliced using the parameters listed in Table 4.2. A comprehensive list of parameters used can be found in Appendix 10.1. Coupons were staggered diagonally in groups of 1, 2, 3, and 4 (Figure 6.1). Runs were repeated enough times to produce at least 4 coupons each (Table 6.1).

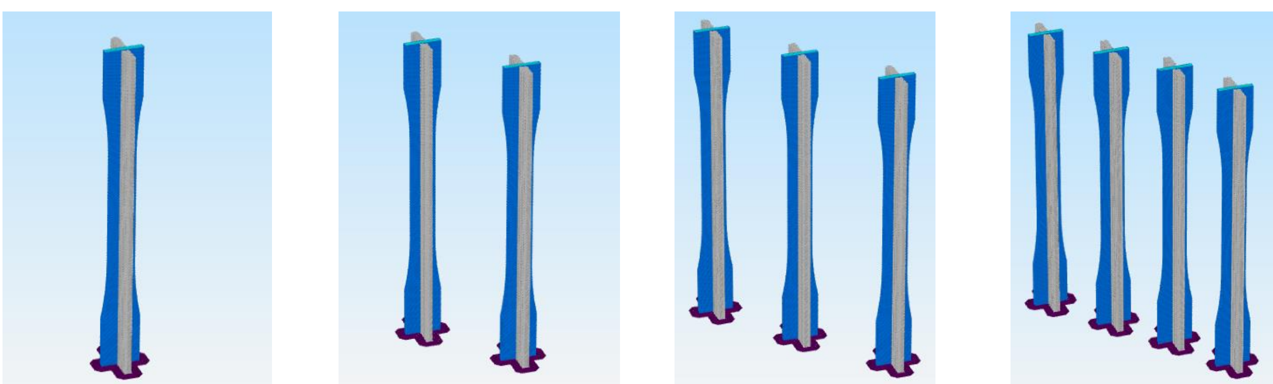

(a) (b) (c) (d)

Figure 6.1. Experimental runs sliced in Simplify3D: run 1 (a), run 2 (b), run 3 (c), and run 4 (d).

Table 6.1. Experimental Runs, Repetitions, and Resulting Coupon Count

Run	Coupon Count	Repetitions	Total Coupons
1	1	5	5
2	2	3	6
3	3	2	6
4	4	1	4

6.2.3 Printer Preparation

Coupons were printed on an AON 3D M2 2020 printer. Prior to printing, a thorough preventative maintenance procedure was carried out following the AON3D documentation [92]. The build plate and chamber were inspected and cleaned using a vacuum cleaner. Microswitches for XYZ-axes and probe were checked and tightened. The Z-axis lead screws and linear shafts were cleaned and re-greased. Finally, the coolant tank was filled and belts were adjusted to the right tension.

The printer was then loaded with a dry spool of filament for coupon printing. Prior to each print, the printer bed and chamber were pre-heated to 180°C and 120°C respectively for 2h. The print area was then probed with the nozzle at 200°C with points placed 20mm apart. The size of the print area varied for each run. The nozzle was then heated to 350°C and bed adhesive was applied to the print area using a paint brush. Upon reaching temperature, 50mm of filament were extruded away from the build plate.

6.2.4 Coupon Printing

A single G-code file was created for each run. Runs were repeated by executing the same file multiple times. The process was closely monitored for the first 2 layers and checked periodically throughout the duration of the print. 3 thermograms were captured for each print at 30%, 50%, and 70% completion following the method developed in Section 5.4.2. At each of these points, the layer time was measured using a stopwatch. The chamber temperature before and after capturing the thermogram was also recorded. Upon print completion, coupons were left to rest for at least 15 minutes before being carefully de-bonded from the build plate using a scraper. They were then labelled and transferred to a dry storage cabinet.

6.2.5 Mechanical Testing

Mechanical testing was conducted on a 100kN Instron electric universal testing machine fitted with tensile grips. Coupons were first dried in a convection oven at 121°C for 48h to satisfy NCAMP's room temperature dry (RTD) testing conditions. Each coupon was measured in length, gauge width, and thickness using a digital caliper. For width and thickness, measurements were taken at 30%, 50%, and 70% of total length and averaged out. Each coupon was then mounted inside the machine and loaded at a rate of 5mm/min. The machine recorded force as a function of displacement. The failure mode was noted by visual inspection. The Instron software was used to automatically compute Young's modulus and ultimate tensile strength. The strains were calculated based on the crosshead displacement.

Figure 6.2. Coupon mounted inside the testing machine.

6.3 Results and Discussion

The data collected during printing, thermography, and mechanical testing was compiled using Excel and Python.

6.3.1 Process Data

Process data included layer time, ambient temperature and humidity, and chamber temperature before and after capturing the thermograms. Readings were done three times per print and collected in an Excel table. The PivotTable feature was used to generate Table 6.2. The average layer time was close to proportional to the number of simultaneous coupons, with deviations due to the additional travel moves required for each additional coupon. Overall, the ambient temperature during the experiment averaged 17.7±0.6°C while relative humidity remained constant at 10% (Table 6.3). After each temperature measurement, the chamber temperature dropped by an average of 10.7±7.3°C (Table 6.4). This is a source of noise which could have caused the printed coupons to momentarily cool down quicker. It is not expected to have had a significant effect due to the high thermal mass of the coupons.

Table 6.2. Layer Time Measurements

Run	Count	Average (s)	Standard deviation (s)
1	15	10.40	0.10
2	18	21.54	0.08
3	18	32.93	0.23
4	12	42.61	0.15

Table 6.3. Environmental Condition Measurements

Run	Temperature avg. (°C)	Temperature std. dev. (°C)	Relative humidity
1	17.1	0.32	10%
2	18.1	0.29	10%
3	17.4	0.332	10%
4	18.1	0.25	10%

*No change recorded in relative humidity throughout the experiment

Table 6.4. Drop in Chamber Temperature After Thermogram Capture

Run	Count	Average (°C)	Standard deviation (°C)
1	15	9.59	2.32
2	18	8.79	2.26
3	18	10.20	3.33
4	12	15.67	2.15
Total	63	10.69	3.56

6.3.2 Thermography Data

Each thermogram was imported into FLIR Thermal Studio to be processed using the method developed in Section High-Temperature Method. Using box tool, the coupon temperature field was selected and exported in CSV format. Using Python, entries in each row were averaged out to a single value. The resulting column vector was used to plot the average surface temperature as a function of vertical distance away from the nozzle in pixels (Figure 6.3). The domain (horizontal span) of each plot is determined by the length of the coupon at the time of measurement. Coupons measured at 50% completion thus have a shorter domain than those measured at 70%, and longer than those measured at 30%.

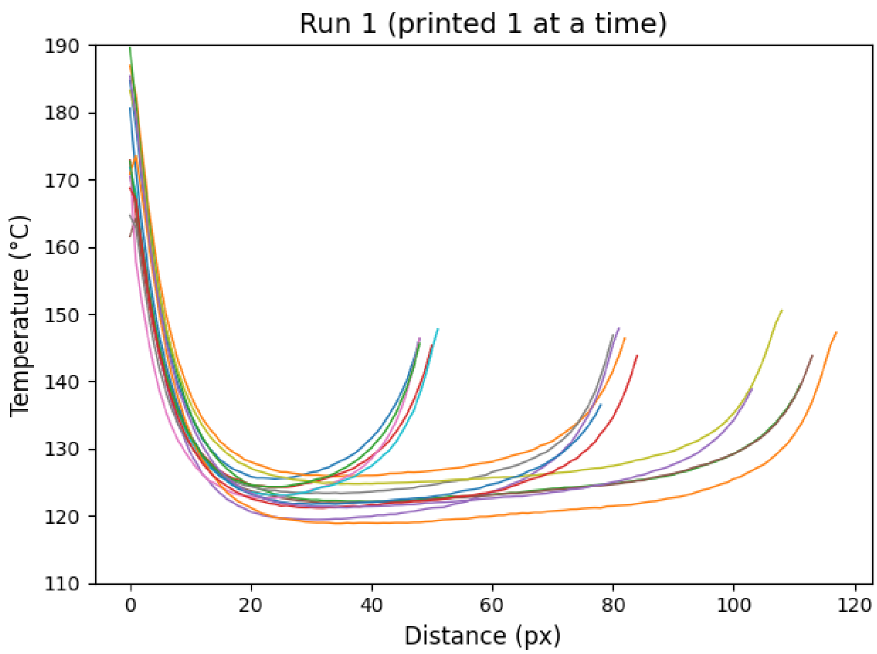

(a)

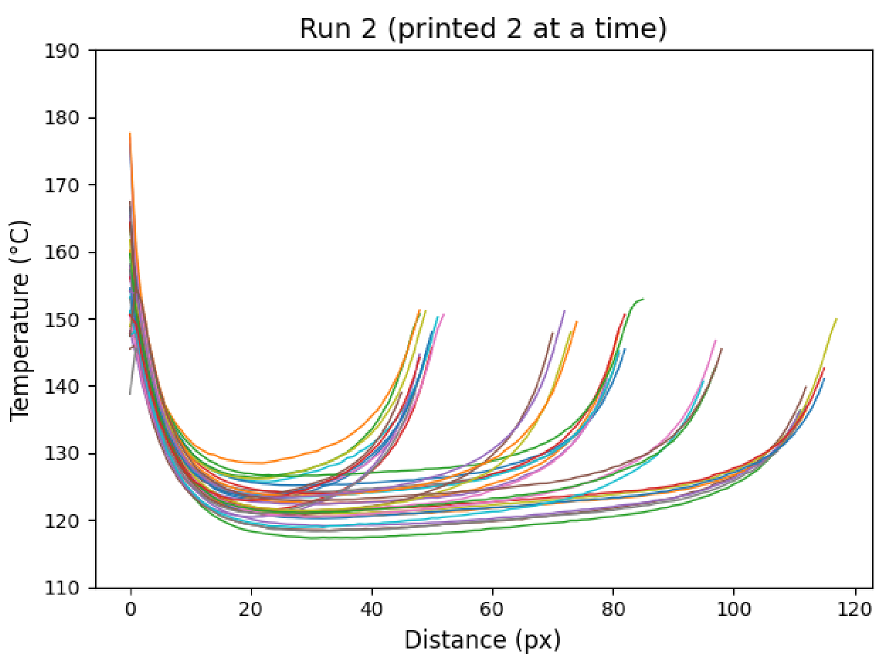

(b)

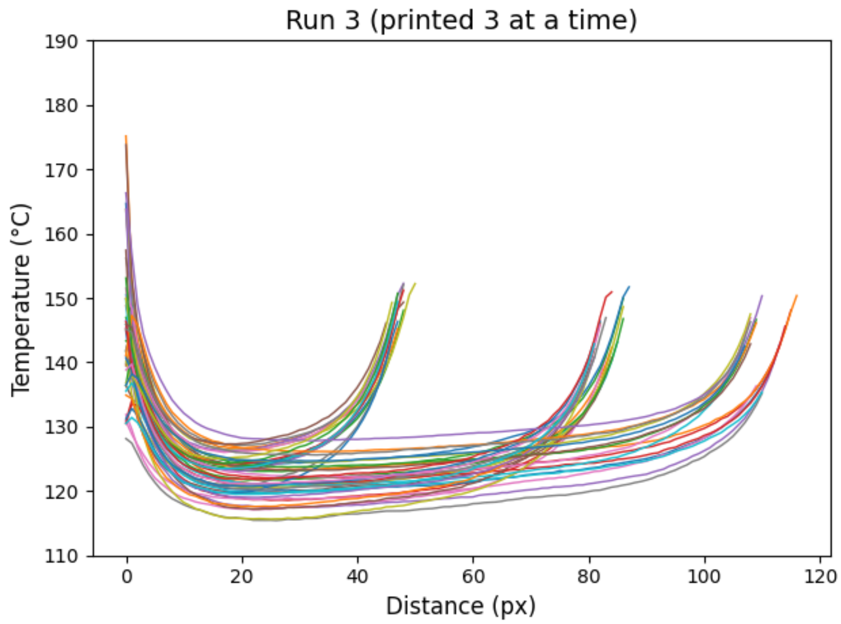

(c)

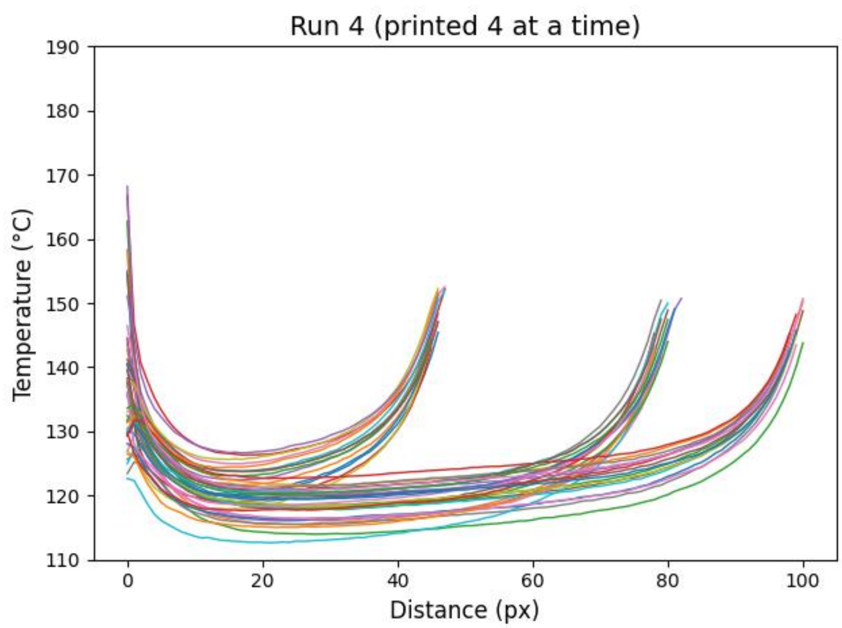

(d)

Figure 6.3. Vertical thermal profiles of coupons printed 1 at a time (a), 2 at a time (b), 3 at a time (c), and 4 at a time (d).

6.3.3 Mechanical Testing

The Instron software was used to generate a report containing results for tensile testing and dimensional accuracy measurements in CSV and PDF formats. The data was copied to an Excel spreadsheet and analyzed using the PivotTable feature. The average and standard deviation for each property were computed (Table 6.5, Figure 6.4).

Table 6.5. Dimensional Accuracy Measurements

Dimension	Count	Average (mm)	Standard dev. (mm)
Thickness	21	3.34	0.03
Width	21	13.09	0.09
Length	21	163.34	0.28

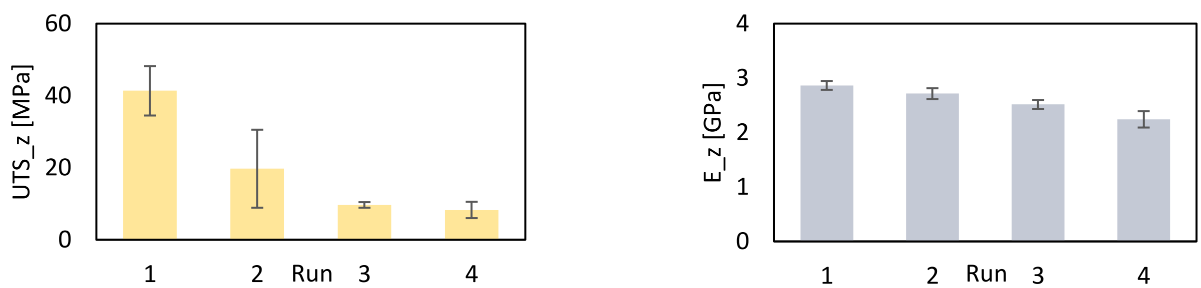

(a) (b)

Figure 6.4. Average ultimate tensile strength (a) and Young's modulus (b) measured for each run.

6.4 ANALYSIS

6.4.1 Process Data

Thermal profiles were analyzed to determine key process parameters possibly correlated with mechanical properties. The first six points—corresponding to a length of 6 px, 6.0±0.3 mm or 30.0±1.5 layers—were used to compute the thermal gradient by linear regression. In addition, the top layer and far field temperatures were respectively taken as the initial and minimum value of each profile. Average values for each run are plotted in Figure 6.5 and Figure 6.6. By inspection, a gradual decrease was observed in top layer temperature and thermal gradient while far field temperature remains stable across runs. This suggests a correlation between layer time and thermal gradient.

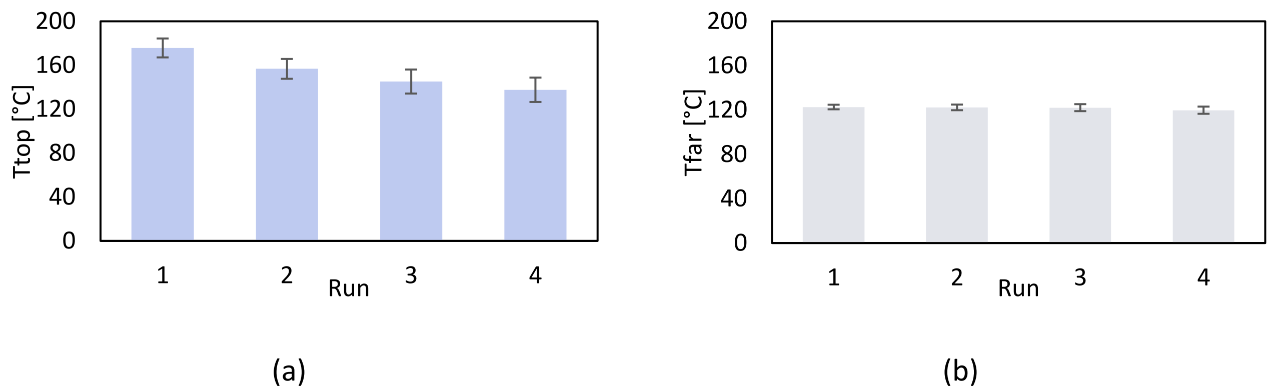

Figure 6.5. Average top layer temperature (a) and far-field temperature (b) for each run.

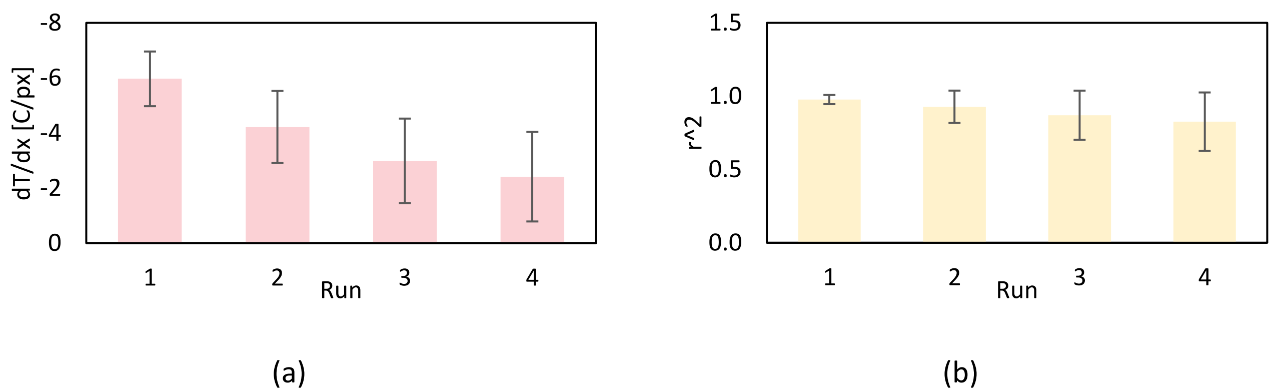

Figure 6.6. Average thermal gradient (a) and associated coefficient of determination (b).

This link was verified by one-way analysis of variance (ANOVA) using an alpha of 0.05. Temperature profiles were grouped according to their run (Table 6.6). The resulting P-value was less than 0.05, indicating a significant difference between the means of each run (Table 6.7).

Table 6.6. Summary of Thermal Gradient Data Analyzed by ANOVA

Groups	Count	Sum	Average	Variance
Run 1	15	-89.5	-5.97	0.99
Run 2	36	-151.8	-4.22	1.71
Run 3	51	-152.2	-2.99	2.37
Run 4	47	-113.4	-2.41	2.64

Table 6.7. Thermal Gradient ANOVA Results

Source of variation	SS	df	MS	F	P-value	F crit
Between groups	177.4	3	59.1	27.3	4.53E-14	2.67
Within groups	313.7	145	2.16			

As layer time increases, there is a corresponding drop in coefficient of determination, indicating higher variability in thermal gradient measurements. This is attributed to nozzle being in a random position when capturing the thermogram (Figure 6.7a). The resulting spread in thermal profiles can also be observed in Figure 4c and 4d. Some profiles have a steeper gradient—between -8 and -4°C/px—since they have just received heat from the nozzle. Others have had time to cool down from the previous layer and have gradients between -4 and 0°C/px. Future experiments should account for nozzle position when capturing thermograms, at it is known to significantly impact the instantaneous thermal gradient in addition to overall layer time.

Another source of variability to be accounted for is the resolution of the thermal camera. Thermograms were captured 0.8 m away from the samples, giving each pixel an approximate size of 1 mm or 5 layers. The temperature value given by the thermogram is therefore the average of the 5 layers contained in that pixel (Figure 6.7b). Since the temperature was observed to change by as much as 6°C/px for low layer times, gradient accuracy could be greatly improved by increasing the resolution. This would provide data on temperature variations between individual layers where bonding takes place. This could be achieved by fitting the camera with a zoom lens to capture a smaller area in greater detail from far away.

With each measurement, the chamber cooled down by an average of 10.69°C. Since the door was never open for more than 15s, this drop recovered within 2±1 min. and isn't expected to have affected the results. However, this factor makes this method unsuitable for continuous thermal monitoring.

(a) (b)

Figure 6.7. Two significant sources of variability encountered in thermal gradient measurements came from nozzle position relative to the cursor (a) and low pixel resolution (b, detail of a).

6.4.2 Mechanical Test Data

Mechanical test data indicated an average decrease of 39% in tensile strength and 7.8% in modulus for each additional printed sample. The link between layer time and mechanical properties was also verified by one-way ANOVA using an alpha of 0.05. Both P-values were less than 0.05, indicating a significant difference between the means of each run (Table 6.8, Table 6.9).

Table 6.8. Modulus ANOVA Results

Source of Variation	SS	df	MS	F	P-value	F crit
Between Groups	0.992	3	0.331	30.96	6.8E-07	3.24
Within Groups	0.171	16	0.011			

Table 6.9. Strength ANOVA Results

Source of Variation	SS	df	MS	F	P-value	F crit
Between Groups	6.23	3	2.08	23.70	4.0E-06	3.24
Within Groups	1.40	16	0.088			

Strength measurements lacked consistency especially for run 2. This is attributed to the nature of the failure mode where the coupon fails at the weakest of all layer interfaces. As such, a higher sample size would be needed to provide reliable strength values.

Increasing the layer time also caused the average top layer temperature to decrease by an average of 7.8% for each additional printed sample. Past studies studying the effect of process temperature on strength only did so for nozzle temperature. Some found that strength was maximized at the highest possible temperature [14, 93] while others found an optimal range [9, 12]. This study is supported by the former two since a higher nozzle temperature would be expected to cause a higher thermal gradient magnitude.

6.4.3 Key Performance Indicators

The KPI used to evaluate process performance and effect of modifying the processing conditions were introduced in Section 3.3. Results are summarized in Table 6.10. Mechanical properties were evaluated based on the performance of Run 1 with coupons printed individually to replicate the NCAMP reference [19]. The resulting tensile modulus was 19.8% above its target while the tensile strength was 30.0% below. Although a multi-parameter DoE would be required to determine optimal process conditions that would maximise strength, it is hypothesised that increasing the nozzle temperature would give the molten filament more time to coalesce and create a stronger bond.

Geometrical accuracy was evaluated based on the average of all printed coupons. Tolerances were calculated by taking ±3 standard deviations about the nominal (average) value for a 99.7% confidence interval. For both thickness and width, the resulting tolerances were well within the required bounds prescribed by ASTM D638 [5].

Table 6.10. Experiment KPI

Property	Target	Result	Ref.
Tensile modulus (Z)	2.392 GPa	2.866 GPa	[19]
Tensile strength (Z)	58.95 MPa	41.33 MPa	[19]
Thickness tolerance	3.2±0.4 mm	3.34±0.10 mm	[5]
Width tolerance	13.0±0.5 mm	13.08±0.25 mm	[5]

7 CONCLUSION

The goal of this work was to develop a framework to evaluate the consistency of processing conditions in open-source FFF via process monitoring. It targets the currently prohibitive cost of certification for non-critical flying parts made with FFF. Process monitoring strategies are needed to demonstrate the structural equivalency between test parts and flying parts.

A review of the literature helped identify monitoring methods to evaluate and improve part quality. IR thermography was ultimately chosen due to its ability to provide a full field reading of the print's temperature profile, gradient, and cooldown rate. In terms of mechanical testing, standard test plans for open-source FFF have yet to be developed. ASTM D638 is still the current benchmark, although printability issues of coupons indicate the need for standards tailored to FFF. It was also found that interlayer mechanical properties were sensitive to processing conditions and had to be tightly controlled to ensure adequate strength of flying parts.

Based on these findings, layer time and thermal gradient were hypothesized to play a key role in resulting interlayer properties by affecting the heat transfer and degree of coalescence between printed layers. A methodology was developed to manufacture FFF parts and evaluate their quality using key performance indicators (KPI).

The initial process evaluation phase revealed defects to correct to successfully print complex parts. Critical parameters were found and tuned to reliably print vertical tensile coupons. Thermal monitoring strategies were developed for low and high temperature printing. The AON3D M2 machine had some reliability issues which were mitigated through hardware and toolpath improvements.

The developed thermal monitoring strategy was used to characterize the effect of thermal gradient on interlayer tensile properties. Printing coupons in batches of different sizes was an effective way of varying the layer time and thermal gradient without altering the print parameters. A significant correlation was found between layer time, thermal gradient, and interlayer tensile strength. The results obtained from this experiment are sensitive to external factors which must be understood to evaluate the reliability of the results and improve the method for future experiments. Notably, it was found that nozzle position had a strong effect on the temperature profile of coupons, causing variability in readings.

The final KPI satisfied geometrical accuracy requirements. The modulus target was exceeded, but that for strength was lower. A DoE where print parameters are varied individually could potentially provide better insight into how to maximise mechanical properties. A significant challenge faced in this work was the narrow processing window of high temperature FFF materials such as ULTEM 9085. Such a DoE would require careful selection of parameter levels to ensure coupons are printed reliably within the studied range.

The ASTM D638 tensile coupon presents some printability issues but remains the geometry of choice for evaluating the impact of process conditions on mechanical properties. Before an AM-specific coupon is agreed upon, it remains the geometry of choice to evaluate tensile properties in each direction.

8 FUTURE WORK

Significant work is still required to fully benefit from the power of process monitoring in FFF. The following recommendations focus on improving the thermal monitoring strategy, integrating more sensors, and developing models to predict part quality based on process data.

There is a challenge in performing thermography while printing materials requiring a heated chamber. Since the FLIR T420 has a maximum operating temperature of 50°C, it cannot be placed inside the 120°C chamber when printing ULTEM 9085. Moreover, the double-pane glass and Lexan (PC) window of the AON3D M2 is IR opaque. As a result, thermal images cannot be captured through it. If continuous monitoring is to be implemented, an apparatus must be developed to either cool down the camera mounted inside the printer (Figure 8.1a) or have an IR transparent window to allow the camera to be mounted externally (Figure 8.1b). Continuous monitoring would be better suited to capture the effect of nozzle position on temperature profiles which was found to be a significant source of variability in the present work. In addition, experimenting with different lens types could lead to better resolution and more refined temperature data. With such equipment, the experiment in Chapter 6 could be repeated while collecting continuous temperature data as function of both space and time. A temperature profile plot could be generated for each coupon with time on the x-axis, vertical position on the y-axis and temperature on a colour scale. This would provide a clearer visualization of temperature evolution in time both on the scale of each layer and the entire print.

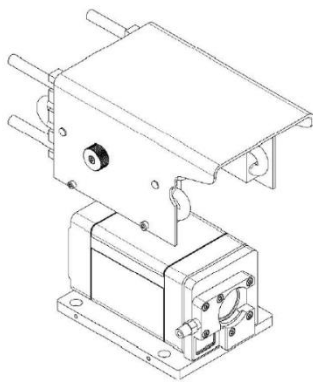

(a)

(b)

Figure 8.1. Two alternatives for minimally invasive in-situ thermal monitoring: a water-cooled enclosure [94] (a) and an infrared-transparent window [95] (b).

Although this work demonstrated the benefits of thermal monitoring, integrating additional sensors could enable features such as fault detection and correction. A simple optical camera mounted externally would allow remote monitoring of prints and inform emergency stop procedures via manual inspection or computer vision. As demonstrated by Kousiatza and Karalekas [38], motor current sensors can detect surges associated with nozzle clogging and print failure. Continuous current data could provide data on extrusion quality and monitor nozzle wear.

Implementing continuous monitoring strategies with different types of sensors can quickly result in significant data processing and management challenges. Future work should focus on streamlining the flow of data and automating post-processing to provide useful insights to inform corrective behaviour, for example, deviation feedback via machine learning. Traceability should be a core objective of such an implementation, with the data cloud being sortable by batch, part, process conditions and other relevant categories.

A key purpose of process monitoring is model validation. The complex multiphysical nature of FFF makes purely physics-driven models extremely computationally expensive. Process parameters such as temperature, thermal gradient and layer time could be used as inputs to data-driven models to predict resulting mechanical properties and part quality. They could also be used to validate heat transfer models and evaluate the repeatability of the printing process.

Developing process models able to accurately predict mechanical properties requires extensive mechanical testing. There is a need for a standardized test coupon designed specifically for FFF. Having a geometry that is printable within a wide processing window would help create streamlined DoE to gain maximum insight into the process quickly and at minimal cost. The design should account for the different failure modes which can occur depending on loading direction. Crack-propagation tests designed for brittle failure may be better suited to evaluate interlayer properties. Coupons should also provide information on print quality, to minimise the number of test prints. In metal AM, so-called artifact coupons have been designed to optimize process settings to print complex geometry [88]. An equivalent design for polymer FFF would be useful for systematic tuning through DoE.

Finally, before aerospace FFF parts can be sold commercially, they must undergo testing of their own. When printing parts rather than test coupons, layer times are usually on the order of minutes, not seconds. As a result, the effects observed in this work should be studied at higher layer times, first by printing more coupons at once, and then by printing more complex geometries.

9 REFERENCES

[1] Stratasys. (2021). *F900*. Available: https://www.stratasys.com/en/3d-printers/printer-catalog/fdm-printers/f900-printer/

[2] Stratasys. (2021). *ULTEM 9085 resin*. Available: https://www.stratasys.com/en/materials/materials-catalog/fdm-materials/ultem-9085/

[3] G. D. Goh, Y. L. Yap, S. Agarwala, and W. Y. Yeong, "Recent Progress in Additive Manufacturing of Fiber Reinforced Polymer Composite," *Advanced Materials Technologies,* vol. 4, no. 1, p. 1800271, 2019/01/01 2019.

[4] Y. Zhao, K. Zhao, Y. Li, and F. Chen, "Mechanical characterization of biocompatible PEEK by FDM," *Journal of Manufacturing Processes,* vol. 56, pp. 28-42, 2020.

[5] *ASTM D638: Standard test method for tensile properties of plastics*, 2010.

[6] *ASTM D790: Standard test method for flexural properties of unreinforced and reinforced plastics and electrical insulating materials*, 2010.

[7] *ASTM D2344: Standard Test Method for Short-Beam Strength of Polymer Matrix Composite Materials and Their Laminates*, 2016.

[8] *ASTM D5045: Standard Test Methods for Plane-Strain Fracture Toughness and Strain Energy Release Rate of Plastic Materials*, 2017.

[9] F. Ning, W. Cong, Y. Hu, and H. Wang, "Additive manufacturing of carbon fiber-reinforced plastic composites using fused deposition modeling: Effects of process parameters on tensile properties," *Journal of Composite Materials,* vol. 51, no. 4, pp. 451-462, 2017/02/01 2016.

[10] K. Fayazbakhsh, M. Movahedi, and J. Kalman, "The impact of defects on tensile properties of 3D printed parts manufactured by fused filament fabrication," *Materials Today Communications,* vol. 18, pp. 140-148, 2019.

[11] J. M. Chacón, M. A. Caminero, E. García-Plaza, and P. J. Núñez, "Additive manufacturing of PLA structures using fused deposition modelling: Effect of process parameters on mechanical properties and their optimal selection," *Materials & Design,* vol. 124, pp. 143-157, 2017/06/15/ 2017.

[12] S. Berretta, R. Davies, Y. T. Shyng, Y. Wang, and O. Ghita, "Fused Deposition Modelling of high temperature polymers: Exploring CNT PEEK composites," *Polymer Testing,* vol. 63, pp. 251-262, 2017/10/01/ 2017.

[13] M. F. Arif, S. Kumar, K. M. Varadarajan, and W. J. Cantwell, "Performance of biocompatible PEEK processed by fused deposition additive manufacturing," *Materials and Design,* vol. 146, pp. 249-259, 2018.

[14] N. Aliheidari, R. Tripuraneni, A. Ameli, and S. Nadimpalli, "Fracture resistance measurement of fused deposition modeling 3D printed polymers," *Polymer Testing,* vol. 60, pp. 94-101, 2017/07/01/ 2017.

[15] C. Davies *et al.*, "Proceedings of the Sixth Additive Manufacturing Composite Materials Handbook Meeting," Composite Materials Handbook (CMH-17), 2021.

[16] P. Jonas and J. Tomblin, "Polymer Additive Manufacturing Materials, Machine, Processing and Quality Requirements Specification for ULTEM ™ 9085 and Stratasys Inc. Fortus 900mc Machine," National Center for Advanced Materials Performance, 2021.

[17] R. Andrulonis and J. Tomblin, "ULTEM Material Specification," National Center for Advanced Materials Performance, 2021.

[18] R. Lovingfoss, R. Andrulonis, and J. Tomblin, "ULTEM Material Slash Specification," National Center for Advanced Materials Performance2021.

[19] M. Man and K. Carney, "Stratasys Certified ULTEMTM 9085 Fortus 900mc Additively Manufactured Polymer Material Qualification Data Report," National Center for Advanced Materials Performance, 2020.

[20] E. Clarkson, "Stratasys Certified ULTEM™ 9085 Fortus 900mc Additively Manufactured Polymer Material Qualification Statistical Analysis Report," National Center for Advanced Materials Performances, 2019.

[21] *ASTM E1356-08: Standard Test Method for Assignment of the Glass Transition Temperatures by Differential Scanning Calorimetry*, 2014.

[22] *ASTM D7191-18: Standard Test Method for Determination of Moisture in Plastics by Relative Humidity Sensor*, 2019.

[23] *ASTM D1238-10: Standard Test Method for Melt Flow Rates of Thermoplastics by Extrusion Plastometer*, 2013.

[24] *ASTM E831-05: Standard Test Method for Linear Thermal Expansion of Solid Materials by Thermomechanical Analysis*, 2017.

[25] *ASTM D7028-07: Standard Test Method for Glass Transition Temperature of Polymer Matrix Composites by Dynamic Mechanical Analysis*, 2016.

[26] *ASTM D695-15: Standard Test Method for Compressive Properties of Rigid Plastics*, 2016.

[27] *ASTM D5379: Standard Test Method for Shear Properties of Composite Materials by the V-Notched Beam Method*, 2019.

[28] *ASTM D256-10: Standard Test Methods for Determining the Izod Pendulum Impact Resistance of Plastics*, 2018.

[29] *ASTM D5766: Standard Test Method for Open-Hole Tensile Strength of Polymer Matrix Composite Laminates*, 2018.

[30] *ASTM D6742: Standard Practice for Filled-Hole Tension and Compression Testing of Polymer Matrix Composite Laminates*, 2017.

[31] *ASTM D6484: Standard Test Method for Open-Hole Compressive Strength of Polymer Matrix Composite Laminates*, 2020.

[32] *ASTM D5961: Standard Test Method for Bearing Response of Polymer Matrix Composite Laminates*, 2017.

[33] M. Moretti, F. Bianchi, and N. Senin, "Towards the development of a smart fused filament fabrication system using multi-sensor data fusion for in-process monitoring," *Rapid Prototyping Journal,* vol. 26, no. 7, pp. 1249-1261, 2020.

[34] B. G. Compton, B. K. Post, C. E. Duty, L. Love, and V. Kunc, "Thermal analysis of additive manufacturing of large-scale thermoplastic polymer composites," *Additive Manufacturing,* vol. 17, pp. 77-86, 2017/10/01/ 2017.

[35] F. Wang, F. Ju, K. Rowe, and N. Hofmann, "Real-time control for large scale additive manufacturing using thermal images," in *15th IEEE International Conference on Automation Science and Engineering, CASE 2019, August 22, 2019 - August 26, 2019*, Vancouver, BC, Canada, 2019, vol. 2019-August, pp. 36-41: IEEE Computer Society.

[36] K. Pooladvand and C. Furlong, "Thermo-mechanical Investigation of Fused Deposition Modeling by Computational and Experimental Methods," 2017.

[37] K. Pooladvand and C. Furlong, "Computational and experimental characterization of 3D printed components by fused deposition modeling," in *SEM Annual Conference and Exposition on Experimental and Applied Mechanics, 2018, June 4, 2018 - June 7, 2018*, Greenville, SC, United states, 2019, pp. 87-95: Springer Science and Business Media, LLC.

[38] C. Kousiatza and D. Karalekas, "In-situ monitoring of strain and temperature distributions during fused deposition modeling process," *Materials & Design,* vol. 97, pp. 400-406, 2016/05/05/ 2016.

[39] Y. Tlegenov, W. F. Lu, and G. S. Hong, "A dynamic model for current-based nozzle condition monitoring in fused deposition modelling," *Progress in Additive Manufacturing,* vol. 4, no. 3, pp. 211-223, 2019/09/01 2019.

[40] M. Preissler, C. Zhang, M. Rosenberger, and G. Notni, "Approach for Process Control in Additive Manufacturing Through Layer-Wise Analysis with 3-Dimensional Pointcloud Information," in *2018 International Conference on Digital Image Computing: Techniques and Applications, DICTA 2018, December 10, 2018 - December 13, 2018*, Canberra, ACT, Australia, 2018, pp. APRS; Australian Government, Department of Defence, Defence Science and Technology Group; Canon Information Systems Research Australia Pty Ltd (CiSRA); IAPRO; IEEE; UNSW Canberra: Institute of Electrical and Electronics Engineers Inc.

[41] A. Levy, "Engage collaboration on two step laser welding process."

[42] L. R. De Pretto, M. M. Amaral, A. Z. d. Freitas, and M. P. Raele, "Nondestructive evaluation of fused filament fabrication 3D printed structures using optical coherence tomography," *Rapid Prototyping Journal,* vol. 26, no. 10, pp. 1853-1860, 2020.

[43] L. Fang, Y. Yan, O. Agarwal, S. Yao, J. E. Seppala, and S. H. Kang, "Effects of Environmental Temperature and Humidity on the Geometry and Strength of Polycarbonate Specimens Prepared by Fused Filament Fabrication," *Materials,* vol. 13, no. 19, p. 4414, 2020.

[44] Y. Mahmoud and S. Manoochehri, "In-situ temperature monitoring of ABS during Fused Filament Fabrication (FFF) process with varying process parameters," in *47th Design Automation Conference, DAC 2021, Held as Part of the ASME 2021 International Design Engineering Technical Conferences and Computers and Information in Engineering Conference, IDETC-CIE 2021, August 17, 2021 - August 19, 2021*, Virtual, Online, 2021, vol. 3A-2021, p. Computers and Information in Engineering Division; Design Engineering Division: American Society of Mechanical Engineers (ASME).

[45] A. S. Kelkar, N. N. Kumbhar, and A. V. Mulay, "Surface Roughness Measurement of Parts Manufactured by FDM Process using Light Sectioning Vision System," *Journal of The Institution of Engineers (India): Series C,* vol. 99, no. 4, pp. 429-433, 2018.

[46] J. C. Riddick, M. A. Haile, R. V. Wahlde, D. P. Cole, O. Bamiduro, and T. E. Johnson, "Fractographic analysis of tensile failure of acrylonitrile-butadiene-styrene fabricated by fused deposition modeling," *Additive Manufacturing,* vol. 11, pp. 49-59, 2016/07/01/ 2016.

[47] B. Brenken, E. Barocio, A. Favaloro, V. Kunc, and R. B. Pipes, "Fused filament fabrication of fiber-reinforced polymers: A review," *Additive Manufacturing,* vol. 21, pp. 1-16, 2018/05/01/ 2018.

[48] A. Bellini, "Fused deposition of ceramics: A comprehensive experimental, analytical and computational study of material behavior, fabrication process and equipment design," ProQuest LLC, 2002.

[49] H. S. Ramanath, M. Chandrasekaran, C. K. Chua, K. F. Leong, and K. D. Shah, "Modelling of Extrusion Behaviour of Biopolymer and Composites in Fused Deposition Modelling," *Key Engineering Materials,* vol. 334-335, pp. 1241-1244, 2007.

[50] M. Nikzad, S. Masood, I. Sbarski, and A. Groth, "A Study of Melt Flow Analysis of an ABS-Iron Composite in Fused Deposition Modelling Process," *Tsinghua Science & Technology,* vol. 14, pp. 29-37, 06/01 2009.

[51] J. Nixon, B. Dryer, D. Chiu, I. Lempert, and D. I. Bigio, "Three parameter analysis of fiber orientation in fused deposition modeling geometries," *Annual Technical Conference - ANTEC, Conference Proceedings,* vol. 2, pp. 985-995, 01/01 2014.

[52] A. Garcia, "Nozzle geometry effects on fiber orientation," in *SAMPE Conf Proc.*, 2017.

[53] B. P. Heller, D. E. Smith, and D. A. Jack, "Computing Mechanical Properties from Orientation Tensors for Fiber Filled Polymers in Axisymmetric Flow and Planar Deposition Flow," 2016.

[54] J. P. Lewicki *et al.*, "3D-Printing of Meso-structurally Ordered Carbon Fiber/Polymer Composites with Unprecedented Orthotropic Physical Properties," *Scientific Reports,* vol. 7, no. 1, p. 43401, 2017/03/06 2017.

[55] J. Thomas and J. Rodriguez, "Modeling the fracture strength between fused-deposition extruded roads," *Proc. Solid Freeform Fabr. Symp,* pp. 16-23, 01/01 2000.

[56] L. Li, Q. Sun, C. T. Bellehumeur, and P. Gu, "Investigation of Bond Formation in FDM Process," 2002.

[57] Q. Sun, G. M. Rizvi, C. T. Bellehumeur, and P. Gu, "Effect of processing conditions on the bonding quality of FDM polymer filaments," *Rapid Prototyping Journal,* vol. 14, no. 2, pp. 72-80, 2008.

[58] M. Atif Yardimci and S. Güçeri, "Conceptual framework for the thermal process modelling of fused deposition," *Rapid Prototyping Journal,* vol. 2, no. 2, pp. 26-31, 1996.

[59] S. Costa, F. Duarte, and J. Covas, "Towards modelling of Free Form Extrusion: Analytical solution of transient heat transfer," *International Journal of Material Forming,* vol. 1, pp. 703-706, 04/01 2008.

[60] B. Brenken, E. Barocio, A. Favaloro, V. Kunc, and R. B. Pipes, "Development and validation of extrusion deposition additive manufacturing process simulations," *Additive Manufacturing,* vol. 25, pp. 218-226, 2019/01/01/ 2019.

[61] Y. Zhou, T. Nyberg, G. Xiong, and D. Liu, "Temperature Analysis in the Fused Deposition Modeling Process," in *2016 3rd International Conference on Information Science and Control Engineering (ICISCE)*, 2016, pp. 678-682.

[62] A. K. Ravi, A. Deshpande, and K. H. Hsu, "An in-process laser localized pre-deposition heating approach to inter-layer bond strengthening in extrusion based polymer additive manufacturing," *Journal of Manufacturing Processes,* vol. 24, pp. 179-185, 2016/10/01/ 2016.

[63] R. P. Wool and K. M. O'connor, "A theory crack healing in polymers," *Journal of applied physics,* vol. 52, no. 10, pp. 5953-5963, 1981.

[64] L. Bastien and J. Gillespie Jr, "A non‐isothermal healing model for strength and toughness of fusion bonded joints of amorphous thermoplastics," *Polymer Engineering & Science,* vol. 31, no. 24, pp. 1720-1730, 1991.

[65] T.-M. Wang, J.-T. Xi, and Y. Jin, "A model research for prototype warp deformation in the FDM process," *The International Journal of Advanced Manufacturing Technology,* vol. 33, no. 11, pp. 1087-1096, 2007/08/01 2007.

[66] Y. Zhang and Y. K. Chou, "3D FEA simulations of fused deposition modeling process," in *International Manufacturing Science and Engineering Conference*, 2006, vol. 47624, pp. 1121-1128.

[67] P. Hébert, S. Mathieu, D. Gianotta, and C. Basire, "Holistic Multiscale Simulation Approach for Additive Manufacturing of Plastics," 2016.

[68] F. Talagani *et al.*, "Numerical Simulation of Big Area Additive Manufacturing (3D Printing) of a Full Size Car," *Sampe Journal,* vol. 51, p. 27, 07/01 2015.

[69] B. Brenken, E. Barocio, A. Favaloro, and R. B. Pipes, "Simulation of semi-crystalline composites in the extrusion deposition additive manufacturing process," *Science in the Age of Experience,* pp. 90-102, 2017.

[70] K. Yu, Z. Zhang, Z. Zhou, and M. Dai, "Application of the Five-phase S-curve Velocity Model on FDM Three-dimensional Printer," in *5th IEEE Information Technology and Mechatronics Engineering Conference, ITOEC 2020, June 12, 2020 - June 14, 2020*, Chongqing, China, 2020, pp. 1365-1371: Institute of Electrical and Electronics Engineers Inc.

[71] Y. Cheng and M. A. Jafari, "Vision-Based Online Process Control in Manufacturing Applications," *IEEE Transactions on Automation Science and Engineering,* vol. 5, no. 1, pp. 140-153, 2008.

[72] D. Hartmann and H. Van der Auweraer, *Digital Twins*. 2020.

[73] G. Digital, "Minds + Machines: Meet A Digital Twin," ed: GE Digital, 2016.

[74] N. Zobeiry and A. Poursartip, "Theory-Guided Machine Learning for Process Simulation of Advanced Composites," 2021.

[75] S. H. Ahn, C. Baek, S. Lee, and I. S. Ahn, "Anisotropic tensile failure model of rapid prototyping parts-fused deposition modeling (FDM)," *International Journal of Modern Physics B,* vol. 17, no. 08n09, pp. 1510-1516, 2003.

[76] S. W. Tsai, "Double–Double: New Family of Composite Laminates," *AIAA Journal,* vol. 59, no. 11, pp. 4293-4305, 2021.

[77] S. S. Crump, "Apparatus and Method for Creating Three-Dimensional Objects," USA, 1992.

[78] W. J. Swanson, P. W. Turley, P. J. Leavitt, P. J. Karwoski, J. E. LaBossiere, and R. L. Skubic, "High Temperature Modeling Apparatus," 2004.

[79] Stratasys, "Stratasys F900," 2018.

[80] AON3D, "AON-M2 2020," 2020.

[81] R. Tao, "Filament Quality Control Project," 2020.

[82] Ultimaker. (2022). *Ultimaker Cura*. Available: https://ultimaker.com/software/ultimaker-cura

[83] Simplify3D. (2022). *Simplify3D*. Available: https://www.simplify3d.com/

[84] M. Lay, N. L. N. Thajudin, Z. A. A. Hamid, A. Rusli, M. K. Abdullah, and R. K. Shuib, "Comparison of physical and mechanical properties of PLA, ABS and nylon 6 fabricated using fused deposition modeling and injection molding," *Composites Part B: Engineering,* vol. 176, p. 107341, 2019.

[85] AON3D. (2022). *Shrinkage, Residual Stress and Poor Layer Welding in 3D Printing*. Available: https://www.aon3d.com/material-science/shrinkage-residual-stress-and-poor-layer-welding-in-3d-printing/

[86] C. Greer *et al.*, "Introduction to the design rules for Metal Big Area Additive Manufacturing," *Additive Manufacturing,* vol. 27, pp. 159-166, 2019.

[87] T. Hullette and J. O'Connell. (2022). *3D Printer Test Print: The Best Torture Test Models*. Available: https://all3dp.com/2/best-3d-printer-test-print-3d-models/

[88] L. Rebaioli and I. Fassi, "A review on benchmark artifacts for evaluating the geometrical performance of additive manufacturing processes," *The International Journal of Advanced Manufacturing Technology,* vol. 93, no. 5, pp. 2571-2598, 2017/11/01 2017.

[89] B. S. Rupal, R. Ahmad, and A. J. Qureshi, "Feature-Based Methodology for Design of Geometric Benchmark Test Artifacts for Additive Manufacturing Processes," *Procedia CIRP,* vol. 70, pp. 84-89, 2018/01/01/ 2018.

[90] N. Vorkapic, M. Pjevic, M. Popovic, N. Slavkovic, and S. Zivanovic, "An additive manufacturing benchmark artifact and deviation measurement method," *Journal of Mechanical Science and Technology,* vol. 34, no. 7, pp. 3015-3026, 2020/07/01 2020.

[91] Creative Tools. (2020). *3DBenchy*. Available: https://www.3dbenchy.com/

[92] AON3D. (2022). *Preventative Maintenance Guide*. Available: https://docs.aon3d.com/maintenance_overview/maintenance_preventive/

[93] C. S. Davis, K. E. Hillgartner, S. H. Han, and J. E. Seppala, "Mechanical strength of welding zones produced by polymer extrusion additive manufacturing," *Additive Manufacturing,* vol. 16, pp. 162-166, 2017.

[94] Fluke Inc., "ThermoView TV40 Series User Manual," 2019.

[95] Total Temperature Instrumentation Inc. (2022). *Fluke IR Windows*. Available: https://www.instrumart.com/products/36778/fluke-ir-windows

10 Appendix

10.1 Simplify3D Parameters Used to Print ASTM D638 Coupons in ULTEM 9085

Parameter	Value
Nozzle diameter	0.4 mm
Extrusion width	0.4 mm
Retraction distance	0.8 mm
Extra restart distance	0.0 mm
Retraction vertical lift	0.8 mm
Retraction speed	30 mm/s
Coasting distance	0.6 mm
Wipe distance	1.2 mm
Primary layer height	0.2 mm
Top and bottom solid layers	5
Outline shells	5
First layer height	175%
First layer width	113%
First layer speed	50%
Brim outlines	10
Outline direction	Inside-out
Support infill percentage	35%
Extra inflation distance	0.2 mm
Support base layers	1
Combine supports every	1 layer
Support horizontal offset	0.2 mm
Support infill angle	-45°
Nozzle temperature	350°C
Bed temperature	180°C
Chamber temperature	120°C
Print speed	30 mm/s
Outline, infill and support underspeed	100%
X/Y axis speed	100 mm/s
Z axis speed	10 mm/s
Stop printing at height	165 mm
Infill density	100%
Infill pattern*	Concentric

* Other infill parameters not specified since 5 outline shells result in a fully dense part.